Clouds and precipitation in the initial phase of marine cold air outbreaks as observed by airborne remote sensing

Imke Schirmacher[1], Sabrina Schnitt[1], Marcus Klingebiel[2], Nina Maherndl[2], Benjamin Kirbus[2], André Ehrlich[2], Mario Mech[1], and Susanne Crewell[1]

[1]Institute for Geophysics and Meteorology, University of Cologne, Cologne, Germany
[2]Institute for Meteorology, Leipzig University, Leipzig, Germany

Correspondence: Imke Schirmacher (imke.schirmacher@uni-koeln.de)

Abstract. Marine cold air outbreaks (MCAOs) strongly affect the Arctic water cycle and, thus, climate through large-scale air mass transformations. The description of air mass transformations is still challenging, partly because previous observations do not resolve fine scales, particularly for the initial development of an MCAO, and lack information about the thermodynamical evolution starting over sea ice and continuing over open ocean and associated cloud microphysical properties. Therefore, we focus on the crucial initial development within the first 200 km over open water for two case studies in April 2022 during the HALO-(AC)³ campaign. The two events, just three days apart, belong to a particularly long-lasting MCAO and occurred under relatively similar thermodynamic conditions. However, for the first event, colder airmasses from the central Arctic led to an MCAO index twice as high as for the second event, though both events were stronger than the climatological 75th percentile for that period.

The evolution and structure were assessed by flight legs crossing the Fram Strait multiple times, sampling perpendicular to the cloud streets. Airborne remote sensing and in-situ measurements were used to build statistical descriptions of the boundary layer, dynamics, clouds, and precipitation. For this purpose, we established a novel approach based solely on radar reflectivity measurements to detect roll circulation that forms cloud streets. The two cases exhibit different properties of clouds, riming, and roll circulations though the width of the roll circulation is similar. For the stronger event, cloud tops are higher, more liquid-topped clouds exist, the liquid water path, mean radar reflectivity, precipitation rate, and precipitation occurrence have increased, and riming is active. The variability of rime mass has the same horizontal scale as the roll circulation, implying the importance of roll circulation on cloud microphysics and precipitation.

Boundary layer and cloud properties evolve with distance over open water, as seen by, e.g., cloud top height rising. In general, cloud streets form after traveling 15 km over open water. After 20 km, this formation enhances cloud cover to just below 100 %. After around 30 km, precipitation forms, though for the weaker event, the development of precipitation is shifted to larger distances. Within our analysis, we developed statistical descriptions of various parameters (i) within the roll circulation and (ii) as a function of distance over open water. In particular, these detailed cloud metrics are well suited for the evaluation of cloud-resolving models close to the sea ice edge to evaluate their representation of dynamics and microphysics.

1 Introduction

Marine cold air outbreaks (MCAOs) are accompanied by strong air mass transformations. During Arctic MCAOs, cold and dry air flows from the ice-covered central Arctic southward over the open ocean. There, cloud streets form that are well visible in satellite images and transform to cellular convection downstream under extreme surface heat fluxes (Brümmer, 1996). Especially over the open ocean, cloud streets have important implications on the radiative surface energy budget due to their high albedo induced by liquid cloud tops (Geerts et al., 2022). Moreover, their long lifetimes affect precipitation evolution and characteristics (Morrison et al., 2012) and thus the Arctic water cycle. Arctic MCAOs can also strongly influence the weather in the mid-latitudes (Turner and Marshall, 2011).

The Arctic is a hotspot with respect to climate change, most pronounced by strong surface temperature increases and sea ice decline (Wendisch et al., 2023). Dahlke et al. (2022) also showed significant shifts in the occurrence of MCAOs, i.e., decreases in early winter and increases in late winter, possibly caused by changes in synoptic circulation patterns and feedbacks involving the retreating sea ice. How MCAO characteristics will develop in the future will require improved modeling capabilities (Geerts et al., 2022) and a better process understanding of these air-mass transformations, including cloud phase changes (Pithan et al., 2018). To resolve the mesoscale cloud organization in MCAOs, large-eddy simulations (LES) are required, but especially the transition between organization states is difficult to model as initial conditions, turbulence, cloud microphysics, and large-scale flow interact. Furthermore, small-scale surface heterogeneities in the marginal sea ice zone (MIZ) are important for the formation of rolls (Gryschka et al., 2014) whereby the exposure of air to open water in the MIZ plays an important role (Spensberger and Spengler, 2021). LES studies also highlighted the importance of mixed-phase microphysical processes in preconditioning the transition of cloud organization (Abel et al., 2017; Tornow et al., 2021). Model settings like the employed ice microphysical scheme and model resolution affect the timing of transformation that differs between the models, e.g., when the ice phase is permitted (de Roode et al., 2019), while a higher resolution evokes roll convection at smaller distances to the sea ice edge and increases precipitation amount (Spensberger and Spengler, 2021). However, no consensus has been reached and progress is delayed by the lack of observations to confront models.

First airborne in situ measurements during the Convection and Turbulence (KonTur) experiment (Markson, 1975; Brummer et al., 1982; Brümmer et al., 1985), ARKTIS '88 (Brümmer et al., 1992), '91, and '93 (Brümmer, 1999), and Marginal Ice Zone Experiment (MIZEX; Walter and Overland, 1984) investigated the mesoscale roll convection inside the atmospheric boundary layer (ABL) that is strengthened by thermal instability when air flows from the sea ice over the open water (Atkinson and Wu Zhang, 1996). Brümmer (1996) and Müller et al. (1999) showed how the ABL was modified as a function of distance from the sea ice within the first 300 km under the influence of strong surface heat fluxes from open water. While cloud reflectance measurements by satellites have provided important insights into the geometrical appearance of MCAOs since their beginning, their quantitative use was pioneered by Murray-Watson et al. (2023) who studied cloud development in a quasi-Lagrangian way. Using back trajectories, they investigated cloud properties derived by the Moderate Resolution Imaging Spectroradiometer (MODIS) as a function of time since the air passed the sea ice edge. Liquid water path (LWP) and cloud top height (CTH) increase within the first 10 hours, with the strongest increase in the initial MCAO phase, i.e., the first couple of hours. Further,

they demonstrate that MCAO strength affects the development until 30 h after the air left the ice edge. However, due to retrieval limitations, they only considered liquid-dominated clouds and no information on vertical structure and precipitation is available.

60 The important role of snowfall by MCAOs, producing the majority of snowfall in the North Atlantic, was shown by Mateling et al. (2023) using Cloudsat radar observations. However, Cloudsat sampling is limited by its blind zone of 1 km (Maahn et al., 2014; Schirmacher et al., 2023) and it is unclear whether differences to model precipitation (von Lerber et al., 2022) result from model deficits or instrument limitation.

In summary, there is a clear need for high-resolution cloud observations within MCAO, which are typically only available

65 from ground-based remote sensing measurements at supersites. Therefore, the Cold-Air Outbreaks in the Marine Boundary Layer Experiment (COMBLE) in 2021/2022 (Geerts et al., 2022) established two ground stations at Andenes and Bear Island, Norway, which provided important insights into cloud properties (Mages et al., 2022; Lackner et al., 2023) and supported model evaluation (Geerts et al., 2022). However, these stations were located about 1000 km away from the sea ice edge. Thus, only open and closed cellular convection but no cloud streets have been observed.

70 In this study, we exploit detailed cloud observations taken during the initial MCAO phase close to the ice edge, where rapid development of mixed-phase clouds occurred. We use airborne remote sensing observations that target model evaluation in a statistical sense and suggest suitable metrics for this. The measurements were performed during the HALO-(AC)[3] campaign (Wendisch et al., 2024) that took place over the Fram Strait where MCAOs occur frequently (Dahlke et al., 2022; Mateling et al., 2023; Papritz et al., 2015). We focus on a major MCAO that remained active for more than two weeks (Walbröl et al.,

75 2024). Within this period of northerly flow, just three days apart, two dedicated research flights were performed with active and passive remote sensing instrumentation. The environmental situations during the flights have many commonalities but slightly different flavors, in particular with respect to the cloud properties. Strait flight tracks crossed cloud streets perpendicular to their elongated orientation multiple times to perform high-resolution measurements of cloud and precipitation properties which are not possible from satellite, e.g., see LWP observations by MODIS (Fig. 1c, d). The data cover a fetch, i.e., the distance the air

80 traveled over open water prior to the measurement, up to about 150 km. From these unique measurements, we aim to answer the following questions:

I. What are the differences between the environmental conditions on both flight days, and what are their implications on cloud development?

II. Can we identify characteristic changes in cloud and precipitation properties perpendicular to cloud street orientation,

85 i.e., within the roll circulation?

III. How do roll circulation, cloud, and precipitation properties evolve with fetch in the initial MCAO phase, e.g., up to travel times of four hours?

The paper is organized as follows: First, we introduce the airborne measurements and data (Sect. 2). Second, we describe the methodology that we developed to assign the fetch to each measurement using back trajectories (Sect. 3.1) and the iden-

90 tification algorithm to detect roll circulations from cloud radar measurements (Sect. 3.2). Section 4 describes boundary layer and cloud development during the two flights (Sect. 4.1), characterizes cloud properties within roll circulation (Sect. 4.3) and
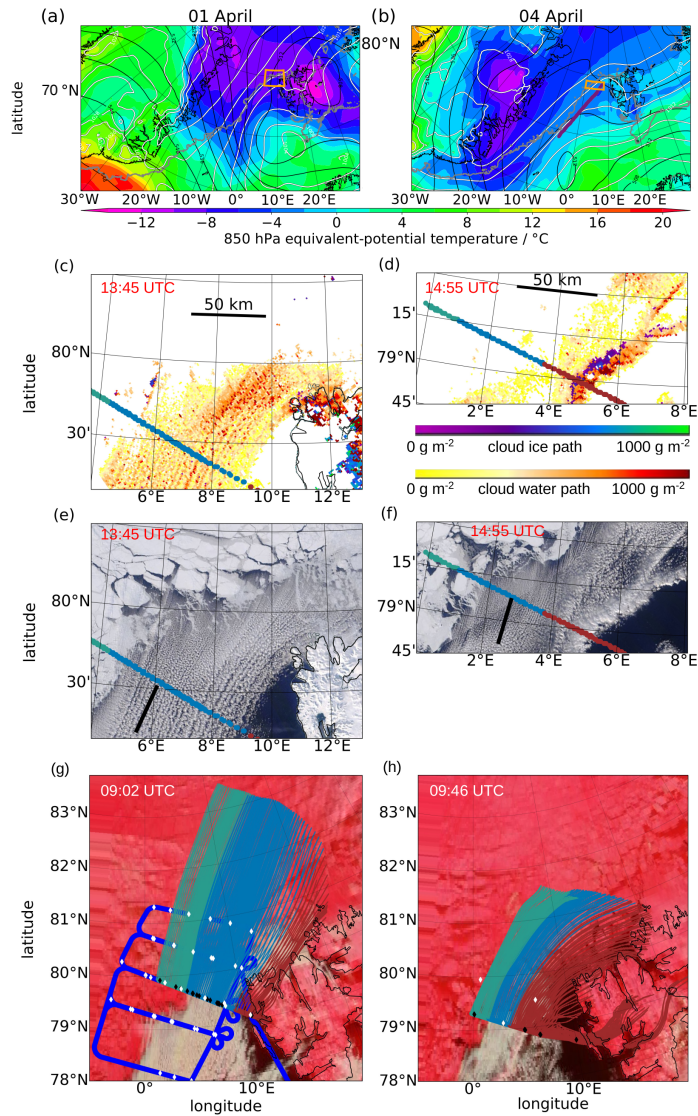
Figure 1. Overview of 01 (left) and 04 April 2022 (right). (a, b) Maps of mean sea level pressure (white contours), 500 hPa geopotential height (black contours), and 850 hPa equivalent-potential temperature (shading) from ERA5 at 12:00 UTC with 15 % sea ice concentration (gray dots), the flight area (orange) shown in c-h, and the convergence line (purple) on 04 April. (c,d) Total cloud water path (Nasa Worldview, 2023a; 1 km resolution) and (e,f) corrected reflectance (Nasa Worldview, 2023b; 500 m resolution) of MODIS Terra on 01 April (13:45 UTC) and 04 April (14:15 UTC). Thick colored dots show P5 track, categorized by the measurement regime (Table 1). Black lines represent the orientation of the cloud streets. (g,h) 12-hour near-surface back trajectories for the P5 measurement locations (colored lines), dropsonde locations (diamonds) of *P5* (black) and *HALO* (white), and the flight path of *HALO* on 01 April 2022 (blue line). Background image from Visible Infrared Imaging Radiometer Suite (VIIRS) (Nasa Worldview, 2023c) at 09:02 UTC on 01 April and 09:46 UTC on 04 April.

the development along fetch (4.4). Finally, Sect. 5 concludes on the questions raised above and discusses pathways for future model evaluation.

2 Data

Airborne measurements from the HALO-(AC)[3] campaign (Wendisch et al., 2021) build the backbone of this study. During this campaign, the High Altitude and LOng-range research aircraft (*HALO*; Ziereis and Gläßer, 2006), the research aircraft *Polar 5* (*P5*) and *Polar 6* (*P6*; Wesche et al., 2016) operated in the North Atlantic sector of the Arctic at altitudes around 10 km, 3 km, and below 3 km, respectively. This analysis mostly focuses on radar, radiometer, lidar, and dropsonde measurements from *P5* that probed MCAO events in their early phase. Dropsonde measurements from *HALO* and in situ observations from *P6* further support the analysis. We limit the analysis to measurements taken over ocean and restrict the remote sensing measurements to straight flight segments that exceed a flight altitude of 2 km to observe clouds from aloft. The focus lies on two *P5* flights, namely on 01 April 2022 (Fig. 1a) and 04 April 2022 (Fig. 1b). To investigate the roll circulation, the flight paths crossed the cloud streets perpendicularly. *P5* probed along the same path back and forth, yielding 6 legs on 01 April (09:08–14:20 UTC) and 4 legs on 04 April (10:06–14:22 UTC).

2.1 Synoptic overview of cases

On 01 and 04 April, the large-scale constellation with a high-pressure system over Greenland and a low-pressure system over Siberia led to the advection of cold air from the central Arctic over the open ocean (Fig. 1a, b) and to cloud street formation (Fig. 1e, f). On 01 April, the center of the cold air at 850 hPa was located over Svalbard. A local near-surface low-pressure system southwest of Svalbard resulted in a near-surface north-easterly flow. With height, the flow turned northerly as indicated by the 500 hPa geopotential (Fig. 1a). On 04 April, contrarily, the cold air at 850 hPa height was shifted more to the west, and the flow at all heights aligned parallel to the sea ice edge over the Fram Strait (Fig. 1b). The easterly flow forced air to ascend over Svalbard, causing a lee effect. Therefore, a larger cloud-free region west of the island appeared, and a convergence line parallel to the ice edge at the transition to the cloudy regime is visible (Fig. 1f). However, note that the flow within our study area might deviate from the large-scale condition. On both days, the MCAO index was stronger than the 75th percentile of the climatology from 1979 to 2022 (Walbröl et al., 2024). While the synoptic conditions are similar for both cases, however, differences in flow directions lead to different MCAO strengths that precondition the evolution over water.

2.2 Airborne instrumentation

Dropsondes: Vaisala Dropsondes RD94 were launched from *P5* and *HALO*. From *P5*, 18 and 14 sondes were launched on 01 and 04 April, respectively. They provide vertical profiles of potential temperature (θ; accuracy=0.2 K), relative humidity (2 %), pressure (0.4 hPa), and horizontal wind components derived from GPS recordings (Vaisala, 2010; George et al., 2021).

  Airborne Mobile Aerosol Lidar (AMALi): AMALi onboard *P5* measures profiles of backscattered intensities at 532 nm (parallel and perpendicular polarized) and 355 nm (not polarized; Stachlewska et al., 2010). The lidar measurements are pro-

cessed with a vertical resolution of 7.5 m and temporal resolution of 1 s. Lidar backscatter is highly sensitive to hydrometeors, especially to liquid, which, in our case, is always super-cooled. Cloud top height (CTH) is obtained for every profile that has

125 consecutive heights with backscatter coefficients exceeding one of cloud-free sections by a factor of five. The CTH is the maximum altitude of these consecutive heights. Further details can be found in Mech et al. (2022a) and Schirmacher et al. (2023).

Microwave Radar/radiometer for Arctic Clouds (MiRAC): The active component of the downlooking airborne MiRAC (Mech et al., 2019) onboard $P5$ consists of a frequency-modulated continuous wave (FMCW) radar that operates at 94 GHz.

130 Additionally, an 89 GHz passive channel accompanies the active measurements. Both measurements are taken with 25° backward inclination of the instruments. While the vertically resolved radar measurements are reconstructed to nadir measurements, the passive measurements represent a slant path. MiRAC measures every second, which corresponds to a horizontal resolution of the equivalent radar reflectivity (Ze) of about 85 m at the ground in flight direction for a typical cruise altitude of 3 km height and ground speed of $80 \, \mathrm{m \, s^{-1}}$. The radar measurements are quality controlled and corrected for surface clutter, and aircraft

135 attitude (Mech et al., 2019). The sensitivity and vertical resolution of the cloud radar depend on the chirp settings. During HALO-(AC)[3], the detection limit for the most distant ranges from $P5$ of 3 km was around -45 dBZ and the vertical resolution was 4.5 m close to the aircraft and at most 13.5 m (Mech et al., 2022a). The processing interpolated the vertical resolution to 5 m over the whole profile. A blind zone of 150 m above ground is omitted due to ground clutter (Schirmacher et al., 2023). The accuracy of Ze is about 0.5 dBZ. Attenuation by water vapor (<1 dBZ) and clouds ($\sim$0.6 dBZ) can potentially reduce this

140 accuracy (Schirmacher et al., 2023).

Cloud top height is also derived from the radar profiles at the height of the uppermost radar reflectivity signal above the noise level. Comparing this height with CTH from lidar allows us to assess the supercooled liquid layer thickness (LLT). Here, we exploit the fact that the lidar is more sensitive to particle amount (liquid), whereas the radar is more sensitive to particle size, i.e., ice particles (Ruiz-Donoso et al., 2020). Due to limited vertical resolutions of the instruments and resulting uncertainties

145 in CTH, the CTH of the lidar has to exceed the CTH of the radar by at least 10 m to be defined as liquid topped and thus mixed-phase. For the calculation of hydrometeor depth (D), we take the difference between lidar CTH and the lowest radar signal within a continuous cloud layer. However, if a minor gap in the cloud profile occurs, i.e., the vertical distance between two layers is smaller than 50 m we define only one layer from the lower cloud bottom to the upper cloud top.

We define profiles containing a Ze value higher than -5 dBZ (Schirmacher et al., 2023) in the lowest 500 m (Shupe et al.,

150 2008) as precipitating. Using the Ze-S relation for three bullet rosettes (Kulie and Bennartz, 2009), this value corresponds to a snowfall rate (S) of $0.07 \, \mathrm{mm \, h^{-1}}$. This relation is also used to analyze S close to the ground at 150 m. Note that these S estimates are inaccurate since Z-S relations highly depend on ice habits, which are very variable within cloud streets (Maherndl et al., 2023a; Moser et al., 2023).

The passive channel observes brightness temperatures (TB) primarily influenced by the emission of liquid clouds and the

155 surface. Differences in TB for clear-sky and cloudy situations are used to retrieve LWP over ocean via a regression approach (Ruiz-Donoso et al., 2020). Due to the unknown emissivity of sea ice, LWP is only calculated over open ocean. Depending on atmospheric conditions, the maximum uncertainty is below $30 \, \mathrm{g \, m^{-2}}$ (Ruiz-Donoso et al., 2020). While radar reflectivities

are corrected to nadir profiles, the TB and thus LWP measurements are along the slant path (Mech et al., 2022a). As shown by the lidar backscatter and its strong attenuation close to cloud top and in accordance with Shupe et al. (2008) we assume that most liquid resides in the uppermost few hundred meters of the cloud. Therefore, LWP lags behind the radar observation in time. Based on geometric considerations, we shift the LWP measurements assuming a daily average CTH for cloud streets. Since this average differs for both days, we shift the LWP measurements by different time periods, i.e., 16 and 19 s on 01 and 04 April, respectively, having an estimated maximum error of 4 s. As a result, a good agreement between LWP peaks and profiles of high Ze can be observed.

In situ probes: The *P6* was equipped with three in situ probes, namely the Cloud Droplet Probe (CDP; Lance et al., 2010), Cloud Imaging Probe (CIP; Baumgardner et al., 2011) and Precipitation Imaging Probe (PIP; Baumgardner et al., 2011). The CDP is a forward-scattering optical spectrometer that measures small cloud particles ($2.8–50\,\mu$m). Larger cloud particles are observed by the CIP ($15–960\,\mu$m) and PIP ($103\,\mu$m–6.4 mm) that record shadow images of the cloud particles as the particles pass through the sampling area (Moser et al., 2023). A continuous particle size distribution is derived for calculating rime mass by combining CDP, CIP, and PIP. The CIP and PIP data are processed similarly to previous campaigns (Mech et al., 2022a).

Collocation: On both days, *P5* (remote sensing) and *P6* (in situ) were closely collocated. For the analysis of riming, we use a data subset during which both aircraft flew on straight paths with a time difference between the collocated measurements of less than 5 min, a spatial distance between both platforms below 5 km, and a flight altitude of *P6* between 0.15 and 1.3 km. With this, we reduce the error caused by sampling different air masses with *P5* and *P6* and also by sampling air masses with varying microphysical properties due to changing *P6* locations within the cloud vertical extent. On 01 April, 3971 seconds of collocated observations cover longitudes between 4.5 and 6.5°E corresponding to 25–165 km fetch. On 04 April, only 845 seconds of observations are collocated that are located between 1.5 and 4.5°E and cover fetches between 55 and 165 km, mostly at around 80 km. On 01 April, seven collocated data segments exist with gaps of less than 5 s. These segments cover 39 min at 60–140 km fetch with most measurements concentrated around 7°E longitude.

2.3 Satellite and reanalysis data

For the sea ice concentration (SIC), we use a daily product that merges satellite observations from MODIS and the second Advanced Microwave Scanning Radiometer (AMSR2) at 1 km horizontal resolution (Ludwig et al., 2020). For the analysis, we interpolate the data to a 0.05° x 0.05° latitude/longitude grid. Sea surface temperatures (SST) are obtained from the Arctic Ocean - Sea and Ice Surface Temperature product based upon observations from the Metop–A Advanced Very High Resolution Radiometer (AVHRR). The daily product (Copernicus Marine Service, 2023) has a spatial resolution of 0.05° and covers surface temperatures of ocean, sea ice, and MIZ. Using satellite SST and dropsonde temperature measurements above open water (Fig. 1g, h, black and white dots), we calculate the MCAO index from the difference between the potential temperature (θ) at the sea surface and 850 hPa altitude. Generally, the MCAO index is positive during a MCAO and describes its strength (Papritz et al., 2015; Kolstad, 2017). Over ocean, we moreover calculated surface heat fluxes from the satellite SST data and dropsonde observations at 10 m height based on the Coupled Ocean-Atmosphere Response Experiment (COARE) bulk air-sea flux algorithm (Fairall et al., 2003).

European Centre for Medium-Range Weather Forecasts (ECMWF) reanalysis product version 5 (ERA5; Hersbach et al., 2020) is used to analyze the large-scale environmental conditions and to compute back trajectories using Lagranto (Sprenger and Wernli, 2015). ERA5's temporal, horizontal, and vertical resolution is one hour, 31 km, and 137 model levels from the surface up to the top of the atmosphere, respectively (Kirbus et al., 2023). Note, that most HALO dropsondes have been assimilated in ERA5, leading to an improved performance for our study cases.

3 Analysis and identification approaches

In the following, we describe two approaches we established for analyzing airborne measurements. The first concerns the quantification of the fetch assigned to each measurement (Sect. 3.1). Second, we present a novel method to identify roll circulation from airborne radar reflectivities only (Sect. 3.2).

3.1 Trajectory calculations and fetch

During MCAOs, the warm ocean alters thermodynamic conditions of airmasses within the ABL, which were formed in the central Arctic, by turbulent surface heat and moisture fluxes (e.g., Brümmer, 1996) whenever SIC is below 100 %. We aim to quantify this influence of open water on ABL development. Since it is impossible to calculate integrated surface fluxes along the trajectories with our data, we derive the fetch for each airborne measurement. We follow Spensberger and Spengler (2021) and also account for open water over the MIZ and leads in the ice. For flows unaffected by land masses, travel time over open water and fetch can be linearly converted and are both valid to study. The correlation coefficient between travel time and fetch is 0.99 for all *P5* measurements that are not influenced by land masses and -0.5 for measurements influenced by Svalbard. Therefore, the latter data have been removed from the analysis (see below).

We need to know the air masses' previous path to calculate fetch for each measurement. For this purpose, we compute near-surface Lagrangian back trajectories using Lagranto (Sprenger and Wernli, 2015) with ERA5 wind fields as input. Specifically, we calculate back trajectories for the previous 12 hours for every flight minute and assign them to the observations within each minute. The trajectories originate at the horizontal location of *P5* and at 1000 hPa height corresponding to roughly 300 m above the surface. To investigate the influence of the surface on the air masses, we take a near-surface starting point for the trajectories. Similar to Spensberger and Spengler (2021), we calculate the fetch for every back trajectory by integrating the ratio of open water obtained from MODIS-AMSR2 SIC data (Sect. 2.3) along the back trajectory paths over the previous 12 h until measurement time (0 h):

$$fetch = \int\limits_{s(12\,h)}^{s(0\,h)} (1 - SIC(s))ds \tag{1}$$

Note that due to the resolution of ERA, neighboring trajectories are rather similar (Fig. 1g, h). Differences in fetches between two neighboring trajectories mainly come from differences in SIC along the trajectories. The median of the relative change between two adjacent fetches is 9.6 %.

Table 1. Categorization of *P5* airborne data.

day	description	color	location
01 April	influence by Svalbard	red	longitude>9.08°E
01 April	prior to cloud streets	green	fetch<15 km
01 April	cloud streets	blue	remaining data
04 April	influence by Svalbard and convergence line	red	longitude>3.7°E
04 April	prior to cloud streets	green	longitude<1.7°E
04 April	cloud streets	blue	remaining data

To concentrate on cloud street characteristics during undisturbed MCAO conditions, we limit the analysis to data that did not pass Svalbard at any time and that are not affected by the convergence line on 04 April (Table 1; Fig. 1, non-red dots). The remaining measurements are classified to be either 'cloud streets' (Fig. 1, blue) if radar reflectivities appear regularly or 'prior
225 to cloud streets' (Fig. 1, green). The latter category includes samples taken over and close to sea ice that have fetches less than 15 km on 01 April and longitudes smaller than 1.7°E on 04 April (fetches of about 17 km; Table 1). On 04 April, longitude instead of fetch is used for classification because cloud streets over open ocean and cloud-free conditions over sea ice have both fetches of 17 km. Note that fetch includes contributions from the MIZ (80 % <SIC> 100 %) and open water.

3.2 Roll circulation identification

230 To identify roll circulations from radar measurements, we must rely on indirect information. Previous studies applied spectral analysis to observations of the three wind components, temperature, mixing ratio, and radiative fluxes (Brümmer et al., 1985, 1992; Brümmer, 1999; Walter and Overland, 1984). While vertical velocity cannot be extracted from the airborne Doppler measurements (Mech et al., 2022a), we exploit the fact that due to the vertical motion, cloud particles form to the largest extent at the location of the strongest updraft. Here, frequent saturation with respect to ice and thus the formation of
235 cloud droplets and growth of both liquid and ice particles occurs (Korolev and Field, 2008). In order to account for potential influences by dry entrainment at cloud top (Klingebiel et al., 2015) or precipitation (Morrison et al., 2012) we only consider measurements at the height of 0.7 of the hydrometeor depth (D; Sec. 2.2) for the identification. By using the radar reflectivity at this height ($Ze_{0.7}$), we target the largest ice particles within the profiles and minimize the influence of dry air entrainment/-supercooled liquid water droplets at cloud top and precipitation at the bottom of D. See Appendix A for a discussion about the
240 height selection and a sensitivity analysis.

$Ze_{0.7}$ serves as a proxy for vertical velocity, and we assume that maxima in $Ze_{0.7}$ represent updraft regions, while minima in $Ze_{0.7}$ represent downdraft regions of the roll circulation. For cloud-free areas, we define the downdraft in the area's center. The workflow behind the circulation detection is summarized in Fig. 2. See Appendix A for further details and Table A1 for a sensitivity analysis. Among different configurations, we selected the detection algorithm with the best ratio between
245 determining peaks and ignoring noise. This automated peak detection depends only on the large-scale condition and thus might not determine every maximum of $Ze_{0.7}$ considered by the human eye.
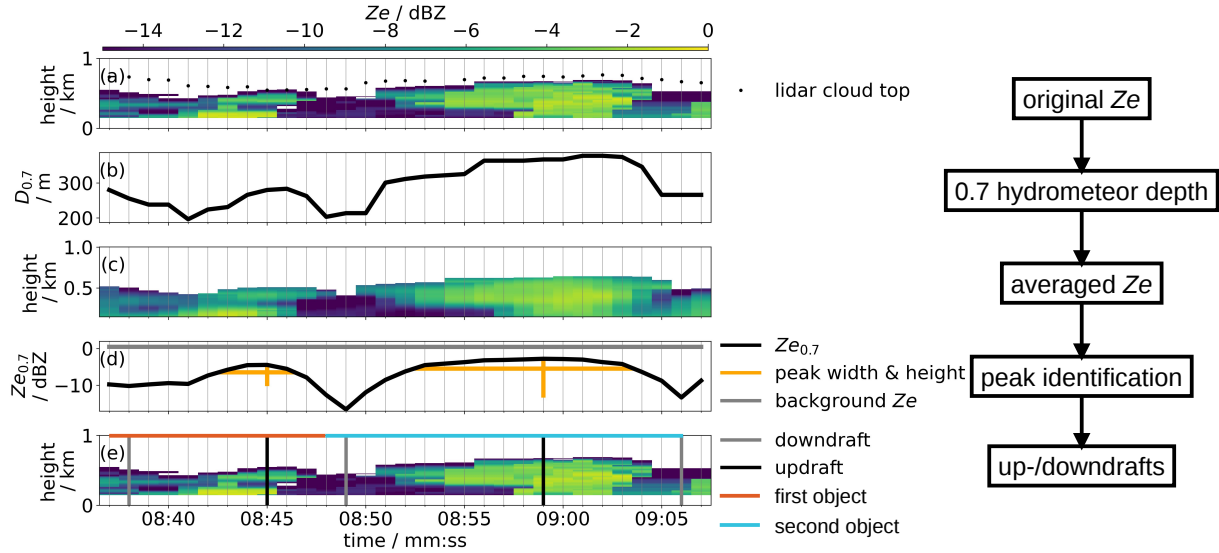
Figure 2. Visualization of roll cloud circulation identification. Time series (30 s) of the equivalent radar reflectivity Ze profiles measured by MiRAC starting at 10:08:37 UTC on 01 April (a), 0.7 of hydrometeor depth ($D_{0.7}$, b), Ze smoothed in space and time (c), smoothed Ze at $D_{0.7}$ (d, black) with its peak width and height (d, orange) and the background Ze (d, gray). The original Ze observations (same as in a), detected up- (black) and downdrafts (gray), and circulation objects (blue, red) are shown in (e). For comparison, the cloud top height observed by the lidar AMALi is displayed (a, black dots). The shown time period covers fetches from 73 to 80 km and corresponds to a flight distance of 7 km.

We only apply the detection algorithm to the 'cloud street' regime as roll convection is invisible to the radar as long as no significant amounts of hydrometeors are present. According to our definition, the maximum updraft (maximum $Ze_{0.7}$) does not necessarily need to be centered between the two detected edges of our roll circulation object. The wavelength of the circulation 250 (λ) is the distance between two identified adjacent downdrafts. The mesoscale circulation is described by the aspect ratio (AR), i.e., the ratio between λ and CTH at the updraft position. In total, we identified 356 and 112 cloud circulation objects in the 'cloud street' regime on 01 and 04 April, respectively.

4 Variability of thermodynamic conditions and cloud street properties

In the following, we first investigate the boundary layer conditions (Sect. 4.1) and the preconditioning by riming (Sect. 4.2). 255 Afterward, we statistically analyze cloud morphological and microphysical properties within the roll circulations for the 'cloud street' regime, (Sect. 4.3) followed by an assessment of cloud and precipitation properties as a function of fetch within the first 170 km (4 h) of the MCAO development (Sect. 4.4).

Table 2. Conditions during 01 and 04 April. BLH and CTH stand for atmospheric boundary layer height, i.e., the inversion height of potential temperature, and cloud top height, respectively.

parameter	source	01 April	04 April
MCAO index	dropsondes	8.6 K	4.6 K
cloud street orientation	MODIS	10°N	5°N
cloud street wavelength	MODIS	2 km	1 km
temperature at cloud top	dropsondes	<-20°C	-20 to -10°C
median cloud street CTH	radar	700 m	300 m
interquartile range of cloud street CTH	radar	530–790 m	250–375 m
BLH trend	dropsondes	4.5 m km^{-1}	2.9 m km^{-1}
mixing ratio trend within 100 km fetch	dropsondes	< doubling	> doubling
driver of wind shear	dropsondes	wind direction	wind speed
cloud street profiles with precipitation	radar	67 %	35 %
cloud street profiles with liquid-topped clouds	radar and lidar	86 %	71 %

4.1 ABL conditioning

First, we investigate how much the ABL conditions differ between the cases, including possible drivers. The influence of the ocean on the ABL through surface sensible and latent heat fluxes is more pronounced on 01 than 04 April (Fig. 3e, f). Dropsondes show maxima of 450 (225) W m^{-2} for sensible (latent) heat fluxes. Over the MIZ, fluxes decrease, and the ratio changes to a higher contribution of the sensible heat flux due to less evaporation over sea ice as also found by Li et al. (2020). Along the whole flight track, ERA5 shows that the sensible heat flux decreases much faster with distance from the sea ice edge on 04 than 01 April (Fig. 3e, f), even though the oceanic conditions, i.e., SST, are similar (Fig. 3a, b). This indicates that the atmospheric conditions differ between the cases, which is especially confirmed for temperature by differences in MCAO fields (Fig. 3c, d). The MCAO index averaged over all dropsondes launched from $P5$ is with 8.6 K stronger on 01 than 04 April (Table 2). Note that although the dropsondes on 01 April were launched further away from sea ice, ERA5 fields show roughly the same factor of two differences over both flight tracks. In general, the fluxes and MCAO indices from ERA5 correspond to dropsonde estimates, except over sea ice where ERA5 seems to overestimate the fluxes. However, the dropsondes resolve finer spatial structures in both parameters.

The cloud condition on 01 April is characterized by cloud streets with an orientation of about 10° to the north (Fig. 1e, black line) and a wavelength of about 2 km with shorter distances between the separated streets close to sea ice. Note that this information is retrieved from MODIS sensors (bands 1, 3, and 4) that have a spatial resolution of at least 500 m. Close to the sea ice edge, the near-surface air of the 'prior to cloud streets' regime shows weak subsidence (Fig. 3g, green track). For the 'cloud street' regime, the air ascends except for fetches between 75 and 120 km (about 7°E longitude; blue track) even though SST and MCAO indices increase (Fig. 3a, c). We suggest that this subsidence, which is visible over the whole atmospheric column (not show n), is provoked by a wave effect induced by Svalbard.
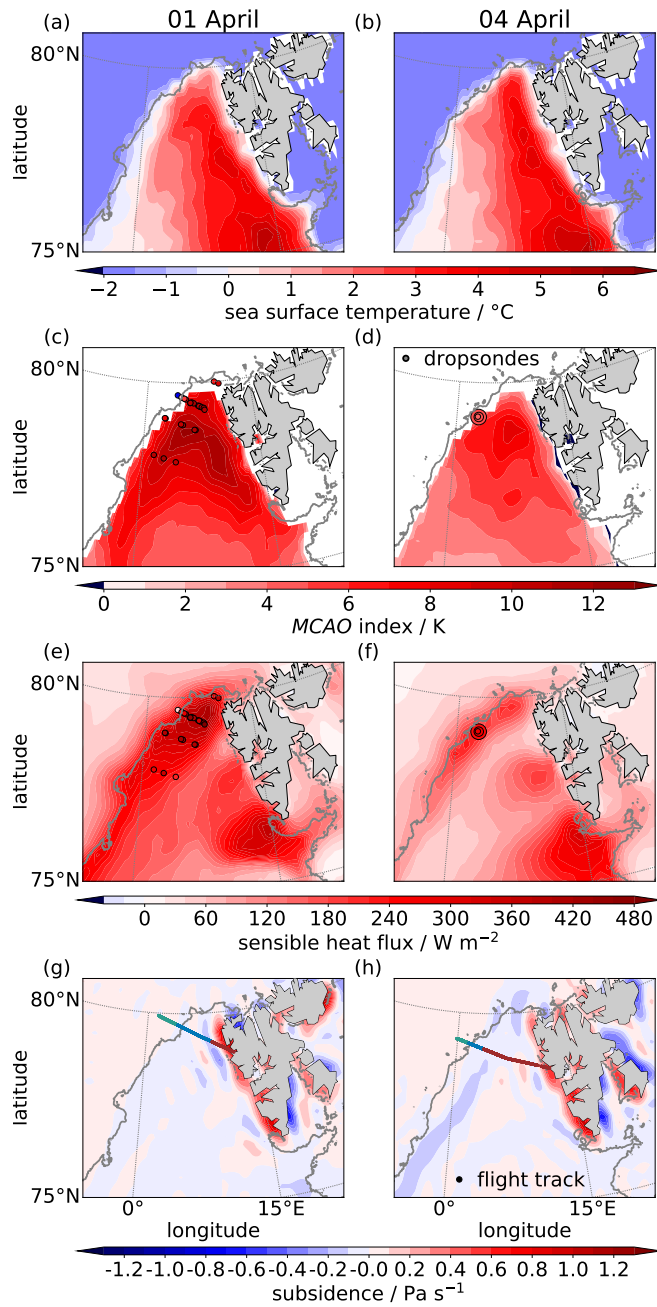
Figure 3. Overview of environmental conditions on 01 April (left) and 04 April (right). Maps of MCAO index (a, b), sea surface temperature (c, d), and subsidence at 1000 hPa (e, f) from ERA5 reanalysis data. Positive subsidence values indicate downward motion. MCAO indices from dropsonde observations are shown as circles (a, b). Flight tracks in (e) and (f) are color-coded according to the measurement categorization (Table 1). The gray lines indicate the 15 % sea ice concentration from ERA5.
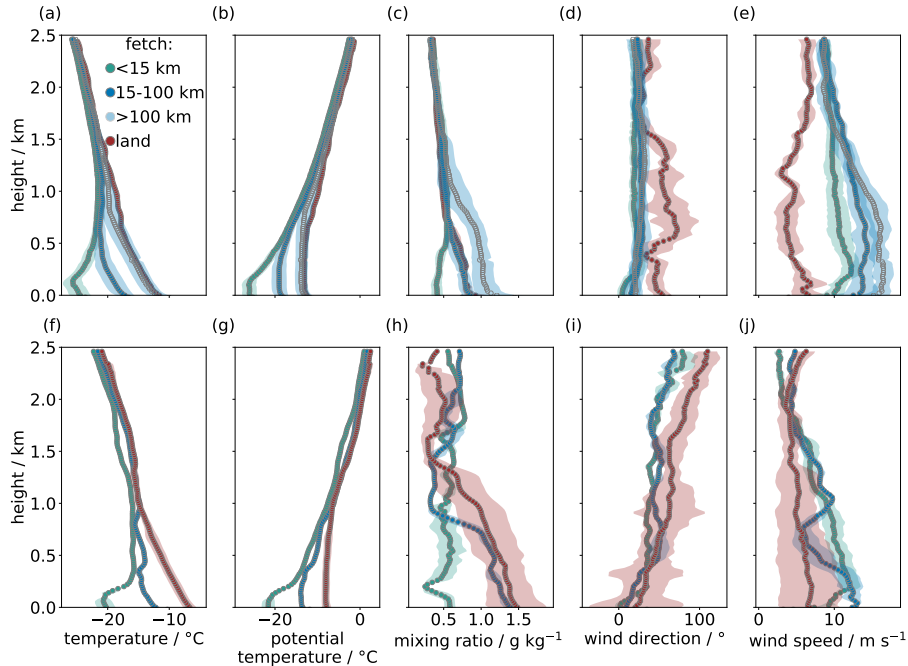
Figure 4. Averaged dropsonde profiles from *HALO* and *P5* of temperature (a, f), potential temperature (b, g), mixing ratio (c, h), wind direction (d, i) and speed (e, j) binned by fetch on 01 April (first row) and 04 April 2022 (second row). The shaded areas represent the standard deviation of each category. The color coding follows the categorization shown in Table 1. On 01 April, the number of dropsondes per category is 27 (<15 km fetch; green), 14 (15-100 km and >100 km fetch; dark and light blue), and 3 (land; red). On 04 April, the number is 3, 4, and 9, respectively.

The thermodynamic state of the ABL is described by mean profiles of dropsondes released from *P5* and *HALO* over sea ice and open water. On 01 April, temperatures are lower than -20°C throughout all altitudes over sea ice (fetch <15 km) and for

280 parts over open water (Fig. 4a). Over sea ice, the surface layers, which are cooled from the ground, and the air above, which is warmed by subsidence, generally develop an inversion. Profiles that were sampled by *HALO* dropsondes over sea ice exhibit a thin (< 250 m deep) ABL. Close to sea ice edge, the depth of the ABL, which is capped by a low-level jet (Fig. 4e) and has a low water vapor mixing ratio (0.5 g kg^{-1}; Fig. 4c), is similar to over closed sea ice (Fig. 4b). The mixing ratio indicates the low background vapor concentration of the polar air mass. With 28°, wind direction is constant with height while the near-surface

285 wind comes from 0°N regardless of surface properties (Fig. 4d). Over open water, the temperatures and, thus, wind speeds within the neutrally-stratified ABL increase with fetch. The boundary layer height (BLH), i.e., the inversion height of the potential temperature θ, doubles within the first 100 km (Fig. 4b). Also, the mixing ratio increases with fetch due to strong surface heat fluxes and turbulent mixing of near-surface air.

On 04 April, the MODIS image shows cloud streets with an orientation of 5° to the north (Fig. 1f, black line) and a wave-

290 length of about 1 km. The air mass ascends at fetches larger than 60 km, i.e., larger fetches compared to 01 April (Fig. 3h). A
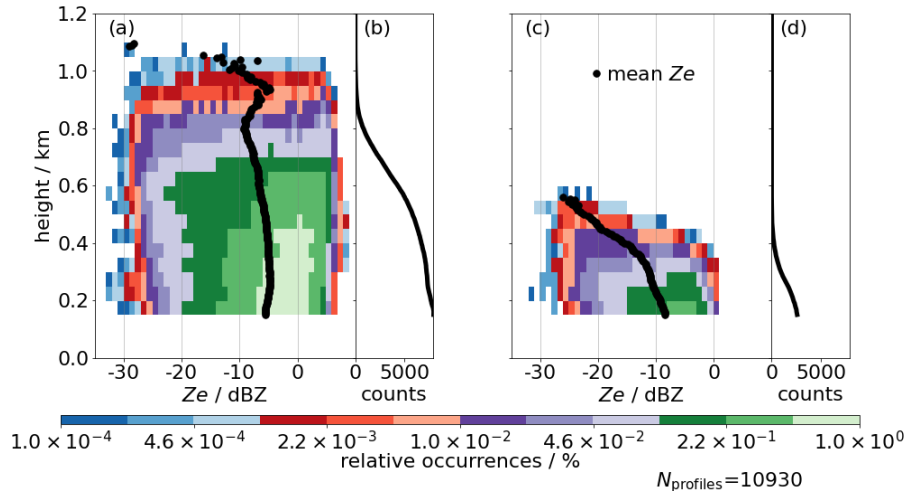
Figure 5. Contoured frequency by altitude diagram (a, c) and absolute counts per altitude (b, d) for all radar reflectivities (Ze) obtained by MiRAC in the 'cloud street' regime on 01 April (a, b) and 04 April (c, d). Moreover, each averaged Ze profile (black dots), and the total number of profiles (N_{profiles}) is displayed.

wave effect is notable within the region affected by the lee effect but not for the analyzed data west of the convergence line. Warmer temperatures on 04 April reveal a difference in air mass between both days: all temperatures below 2 km height lie within -20 to -10°C (Fig. 4f) and θ of the free troposphere is on average by about 5 K higher compared to 01 April (Fig. 4b, g). Furthermore, the mixing ratio of the polar air mass is slightly higher at all heights (Fig. 4c, h). Even though a low-level jet

295   exists at 200 m over sea ice as before (Fig. 4j), flow conditions differ compared to 01 April. A directional shear from northerly wind at the surface to westerly wind occurs at all heights, which is strongest at BLH (Fig. 4i). Although *HALO* dropsondes cannot detect a BLH in the central Arctic (81.3–87.0°N) as it is likely too shallow (not shown), the capping inversion over the sea ice close to its edge is stronger. On 04 April, this inversion weakens less with fetch compared to 01 April due to a layer of warm air above BLH. Together with about half as high ERA5 surface fluxes on 04 April (Fig. 3e, f), this results in a much

300   weaker BLH increase rate averaged over all fetches (Table 2) and a reduction of wind speeds by $5\,\mathrm{m\,s^{-1}}$.

On both days, the radar profiles in the 'cloud street' regime frequently (93 %) exhibit clouds. The contoured frequency by altitude diagrams (Fig. 5) reveals the different cloud and precipitation characteristics of cloud streets between the days: especially, CTH is twice as high on 01 than on 04 April. Furthermore, the mean Ze profile (black dots) is larger at all heights. On 01 April, values larger than -5 dBZ, which are associated with the onset of snowfall, occur at all heights. The shorter the

305   fetch on 01 April, the stronger is the decrease in the mean Ze profile close to the surface (not shown). Thus, near-surface ice particles might experience stronger sublimation on 01 April when the mixing ratio is comparably small and relative humidity with respect to ice below 100 % (not shown). On 04 April, Ze rarely exceeds -5 dBZ even below 500 m reducing the frequency of precipitation compared to 01 April (Table 2). Moreover, mean Ze increases towards the surface, indicating the ongoing
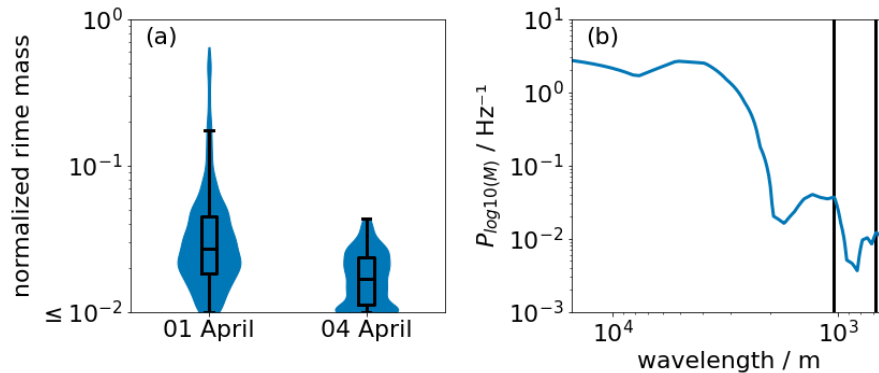
Figure 6. Left: Violin and box plot of the normalized rime mass (M) obtained by the in situ method for collocated flight data of cloud streets on 01 and 04 April. Right: Corresponding power spectrum of M on 01 April with black lines marking important local maxima of the spectrum.

growth process of ice particles. On both days, most cloud streets are liquid-topped (Table 2), which mainly have higher CTH than non-liquid-topped clouds (not shown).

In summary, the MCAO case on 01 April is by a factor of two stronger than 04 April due to colder and drier air masses (Table 2). On both days, wind shear occurs by wind speed changes on 01 and direction changes on 04 April. Contradicting the MCAO index, air subsides close to the surface in the 'cloud street' regime at fetches around 100 km on 01 April due to a wave effect caused by Svalbard.

4.2 Preconditioning by riming

Ice growth affects the boundary layer evolution during MCAOs in several ways, e.g., by reducing cloud liquid water and triggering early and light precipitation, which then cools and moistens the air below the cloud (Tornow et al., 2021). To investigate whether riming preconditions cloud microphysics and precipitation characteristics are already in the initial state of MCAO evolution, we evaluate the strength and variability of riming. In doing so, we use a subset of in situ and remote sensing data within the 'cloud street' regime during which *P5* and *P6* were collocated (Sect. 2). To determine the degree of riming, we calculate the normalized rime mass (M) defined as the rime mass divided by the mass of the size-equivalent spherical graupel particle. Following Maherndl et al. (2023b), two methods are applied. The combined method uses the closure of in situ particle size distributions and Ze simulations obtained from running averages of in situ particle size distributions over 30 s. The in situ method relates M to in situ particle shape measurements only. The results of both retrievals are comparable. However, since the collocation of *P5* and *P6* measurements might be inaccurate, we only show results from the in situ method for which no matching is necessary. Note that our definition of updrafts might bias the following findings.

Considering particles with $M > 10^{-2}$ as rimed, more rimed particles exist on 01 April (97 %) than on 04 April (80 %). The median M of $10^{-1.6}$ on 01 April and $10^{-1.8}$ on 04 April (Fig. 6a) clearly reveals that riming is only significantly active

in cloud streets on 01 April. In particular, normalized rime masses $M > 10^{-1}$ only exist on 01 April. On this day, cloud top
temperatures are colder than or at the low end of temperatures within the dendritic-growth zone (DGZ; -20 to -10°C) and
hence too cold for aggregation to be dominant (Chellini et al., 2022). On 04 April, contrarily, riming is not significant because
cloud top temperatures lie within the DGZ that favors aggregation.

The spatial variability of riming is investigated by linearly detrended and mean-centered power spectra of M obtained during
seven collocated segments (Sect. 2). Edge effects are minimized by applying a Hann window for smoothing. Due to the units
of variance, the power spectrum increases automatically for smaller wavelengths. The averaged power spectrum of M peaks
at about 0.7 and 1.1 km (Fig. 6b). These values roughly correspond to the wavelength λ of cloud streets as seen in the MODIS
images (Fig. 1) and a more detailed comparison with λ detected by the remote sensing measurements will be performed in
Sect. 4.4. For 01 April, we suggest that riming is enhanced in updraft regions, where it results in higher precipitation rates.
Thus, riming, which is only active during the strong MCAO case with cold temperatures, seems to precondition precipitation.
We further analyze the effect of riming on cloud microphysics in the following sections.

4.3 Impact of roll circulation on cloud and precipitation properties

Our measurement strategy across cloud streets allows us to detect the individual roll circulation objects (Sect. 3.2). For the
following statistical assessment, we use objects that have at least five successive radar measurements, i.e., 344 and 109 objects
on 01 and 04 April, respectively, and refer to them as 'clouds'. First, we investigate the location of its updraft center ($Ze_{0.7}$)
within the cloud. As explained before, objects are not necessarily symmetric. However, most clouds form centered around the
updraft of the circulation: around 50 % of the time, maxima of $Ze_{0.7}$ occur within the central tercile of the cloud and only
rarely within the tercile closest to the lateral cloud boundary (7 %).

To characterize how dynamics within roll circulations affect cloud and precipitation properties, these are composited for their
relative distance to $Ze_{0.7}$ (Fig. 7). More precisely, we group cloud properties according to their distance from the maximum
updraft region ($Ze_{0.7}$) into three regions: the central updraft region, the region close to cloud boundary, and the region in
between.

On 01 April, the median of several parameters shows consistent behavior although the variability, expressed by the interquar-
tile distance, is high: CTH increases by 9 % from the cloud boundary until the location of the maximum updraft. In line with
liquid formation within updrafts, LWP increases (22 %). The mean of Ze over each profile (82 %) and S (42 %) increase,
undermining our assumption of the enhanced ice production in updrafts. In contrast, a decrease of LLT (32 %) by 20 m can
be seen, which exceeds the uncertainty of 10 m. We hypothesize that updrafts transport ice particles into higher parts of the
clouds. The mixed-phase region thus increases at the expense of the liquid layer and riming is enhanced (Fig. 4.2). Riming
increases ice particle size, Ze, and S in updrafts. The observed LWP increase in updrafts might indicate that condensation is
more favored than depletion of liquid.

Strong riming events might explain the frequent high extremes of S. Precipitation events do not only intensify at updraft
locations, but with 87 compared to 55 % of the profiles, also more profiles contain precipitation than at cloud boundary. On
01 April, we expect that most ice, indicated by $Ze_{\max}$, occurs at 0.6 of the hydrometeor depth for updraft positions (Fig. 7k).
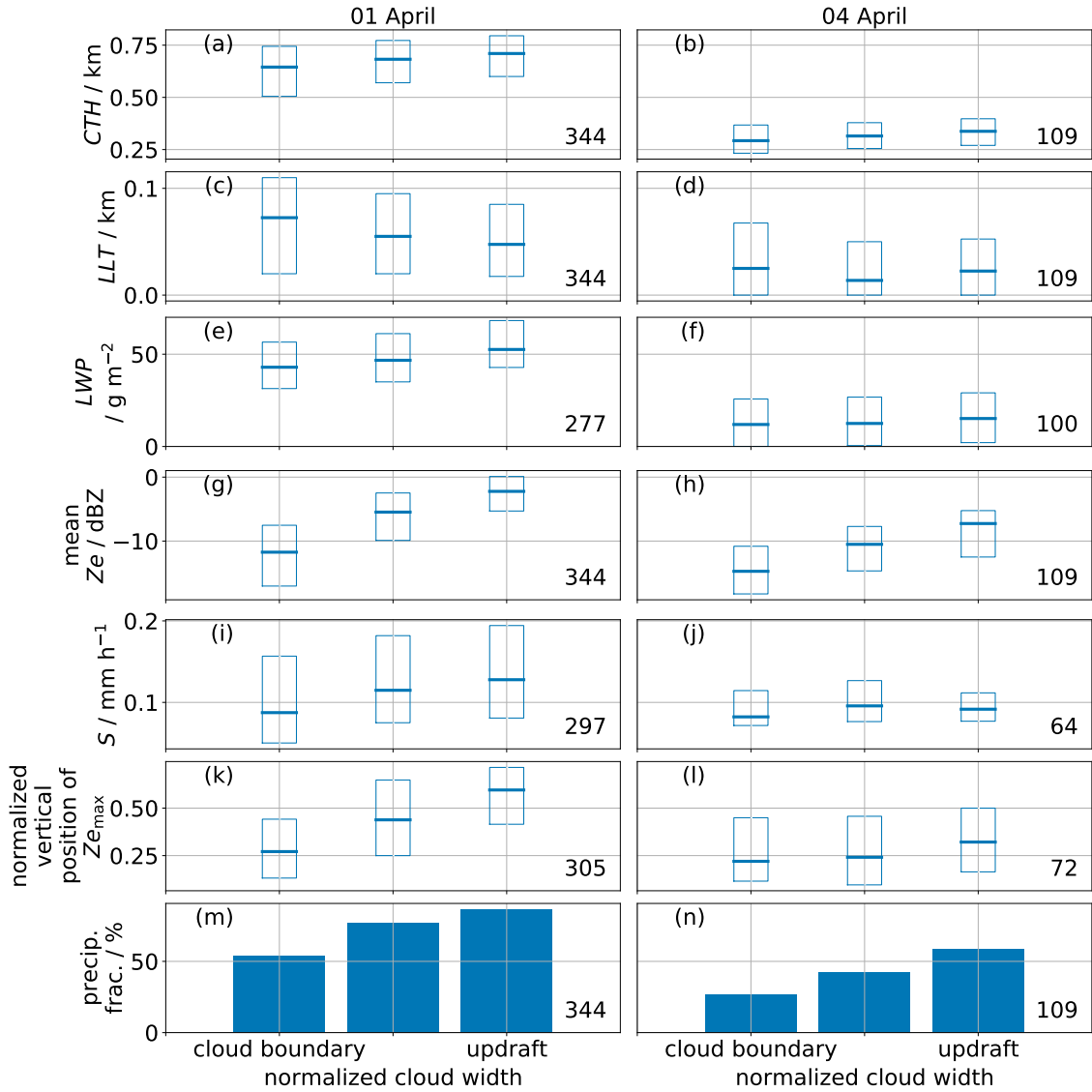
Figure 7. Average composites of cloud and precipitation properties within the normalized distance between lateral cloud boundary and updraft (max $Ze_{0.7}$) for circulation objects within the cloud street regime on 01 April (left column) and 04 April (right column): cloud top height (CTH; a, b), supercooled liquid layer thickness (LLT; c, d), liquid water path (LWP; e), mean radar reflectivity (Ze) over each profile (f, g), snowfall rate at 150 m (S; h, i), vertical position of the maximum Ze for each profile normalized by the hydrometeor depth (j, k), and fraction of precipitating profiles (precip. frac.; l, m). The median (horizontal line) and lower and upper quartile (box edges) are displayed at the boundary of the clouds, the updraft position, and in between. The total number of objects is given for every parameter separately.

Large rimed particles close to cloud top might lift the height compared to the cloud boundary, where most ice is located within the lowest third of the hydrometeor depth.

On 04 April, the absolute increase of CTH and mean Ze within the clouds is about a factor of two lower than on 01 April. Moreover, S and LLT stay constant within the clouds. For all locations, the normalized height with most ice is similar to the one at cloud boundary on 01 April. The smaller MCAO strength seems to explicitly weaken the updraft motion and thus suppress the rise of CTH and the lifting of ice into the liquid layer in updrafts. In updrafts, this prevents riming, which hampers an increase in S and mean Ze, as well as the lifting of the height with most ice. The precipitation fraction is lower compared to 01 April, i.e., only half at cloud boundary, but the increase within the clouds is with 30 percentage points similar.

4.4 Development along fetch

To investigate how the open water surface affects roll circulation and cloud properties, we analyze their evolution over all observed fetches (Fig. 8). The most prominent characteristic of an MCAO event is the rise in boundary layer height driven by the strong heat fluxes when air flows over the relatively warm ocean. Already in the MIZ the evaporation and convection lead to the appearance of first, still unorganized clouds in the 'prior to cloud street' regime, though horizontal cloud cover is low (Fig. 8g). Within the 'cloud street' regime, cloud cover increases quickly, and for fetches larger than 30 km, cloud cover becomes higher than 90%. The comparison of boundary layer height BLH derived from dropsondes and closely located airborne measurements showed that CTH is generally only by 8.5 m lower than BLH, which suggests that we can use CTH as a proxy for BLH. CTH strongly increases with fetch (Fig. 8a) and with distinct differences between 01 and 04 April. On 04 April, the reduced buoyancy within ABL and warm air advection above BLH diminish the median CTH by more than half compared to 01 April to 300 m (Fig. 8b) and the growth rate of CTH with fetch by roughly 55 % (Fig. 8a). Note that this factor of roughly two is also evident in the BLH trend obtained from dropsondes (Table 2). The increase in CTH with fetch is roughly linear, though on 01 April, subsidence (cf. Fig. 3) provokes a stagnation of CTH at around 100 km fetch (2.5 h travel time). For fetches larger than 140 km CTH and also other cloud parameters decrease, probably due to a remaining lee effect caused by Svalbard. Even though ERA5 reanalysis with its coarse resolution shows a rising air mass at these fetches (Fig. 8), we suggest that the air mass subsides and suppresses cloud development.

Next, we focus on the circulation characteristics, i.e., wavelength λ and aspect ratio, of the 'cloud street regime'. Note that bins in fetch with less than 10 roll circulation objects are not analyzed to avoid results being contaminated by outliers. Thus, data gaps around fetches of 50 km exist (Fig. 8c,e). Nevertheless, we can see some development with fetch: λ increases on 01 April (Fig. 8c) from roughly 1 to about 2 km at a fetch of 150 km approaching the width of the cloud streets seen by MODIS (2 km; Sect. 4.1). Because the data used for the spectral analysis of riming are distributed over different fetches it seems likely that the peaks at 0.7 and 1.1 km are linked to cloud streets (Fig. 6). On 04 April, the data only revealed reliable circulation information for fetches smaller than 80 km. For these fetches, λ stays roughly constant and aligns with the cloud street width of the MODIS images (1 km; Sect. 4.1).

The data gaps also affect the analysis of ARs. In fact the large spread between the 5th and 95th percentile hints at the existence of some outlier. There is some evidence that AR decreases with fetch. For fetches larger than 60 km roll circulation is enhanced on 01 April and a constant AR of about 2 is observed. This confirms the model by Brown (1972) stating that AR increases when less energy is available for convection. Regarding median values, λ is similar on both days (around 1.2 km;
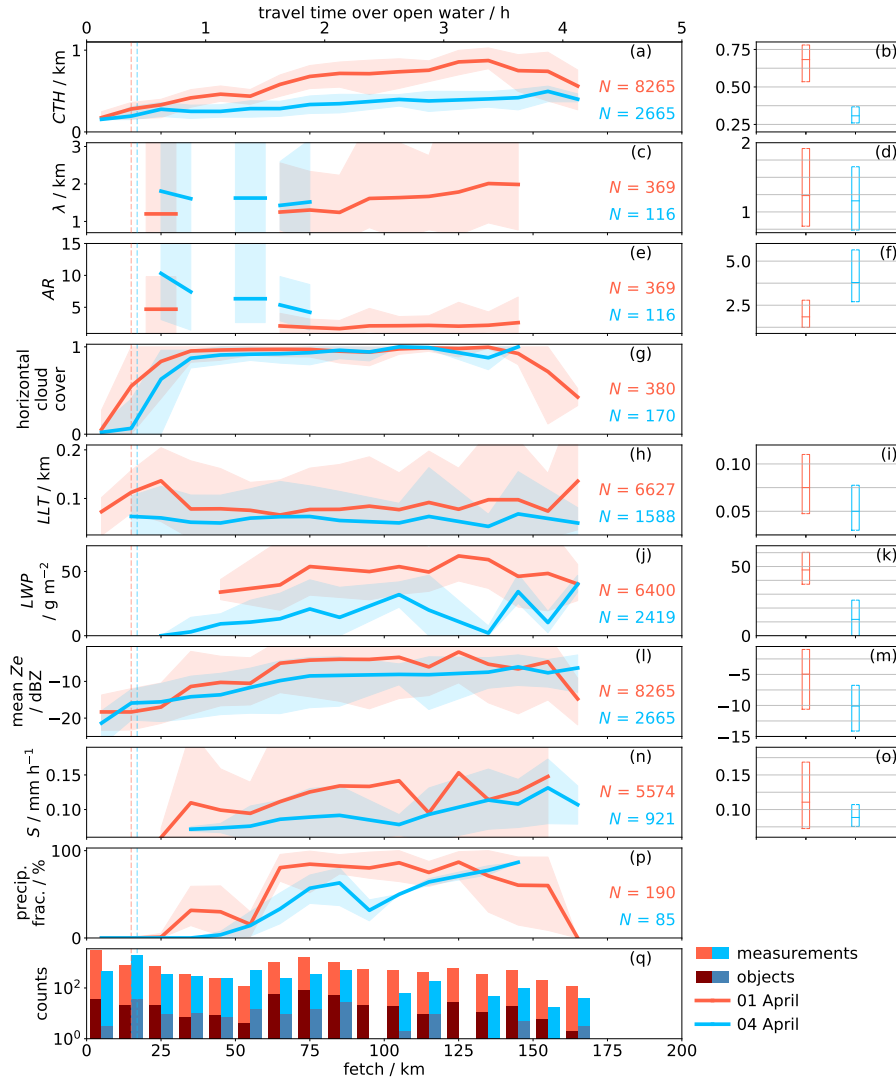
Figure 8. Left: Development of circulation, cloud, and precipitation characteristics with fetch on 01 (red) and 04 April (blue): cloud top height (CTH; a, b), wavelength of the circulation (λ; c, d), aspect ratio of the circulation (AR; e, f), horizontal cloud cover (g), liquid layer thickness (LLT; h, i), liquid water path (LWP; j, k), mean radar reflectivity over each profile (mean Ze; i, m), snowfall rate at 150 m height (S; n, o), precipitation fraction (p), and amount (q) of measured profiles (colored) and identified cloud circulations (gray) per fetch bin. LLT, LWP, and S statistics are only calculated when cloud/precipitation occurs. Lines and shades represent mean values and the 5th and 95th percentile, respectively. The vertical dashed lines indicate the regime change from 'prior to cloud streets' to 'cloud streets' (Sect. 3.1). Right: Boxplots show each distribution's median and interquartile range within the 'cloud street' regime. The total amount of measurements (N) is given for each parameter and day.

Fig. 8d), while CTH is roughly a factor of two larger on 01 April (Fig. 8b). Consequently, the median AR (Fig. 8f) is smaller on 01 April at 1.8 than on 04 April at 3.9.

To investigate how the exposure to open water influences cloud microphysics, we look at the liquid layer thickness LLT (Fig. 8h), LWP (Fig. 8j), mean Ze (Fig. 8l) and S (Fig. 8n). All parameters, with the exception of LLT, show a slight increase with fetch. LWP is significantly higher on 01 April with a median of $50\,gm^{-2}$ compared to $10\,gm^{-2}$ on 04 April. While the latter value is below the absolute LWP error (see Sect. 2 observations for larger fetches exceed this value. The median LLT of 75 (50) m on 01 (04) April points at the dominant presence of liquid layer topped mixed-phase clouds in agreement with Table 2 showing 86% (71%) for the respective days. We attribute the constant LLT with fetch to the fact that both liquid (LWP) and ice (approximated by mean Ze) increase simultaneously, keeping the LLT constant.

The evolution of cloud microphysics with fetch is similar on both days, however, thermodynamic conditions modify the intensity of the parameters. On 04 April, which features warmer temperatures, clouds are more shallow. On this day, 90 % of the profiles containing liquid-topped cloud streets have LLT smaller than 100 m, which is more than on 01 April (70 %). Less supercooled liquid reduces the amount of liquid-topped cloud profiles (Table 2), LWP (Fig. 8k) and LLT (Fig. 8i). The warmer temperature, low amount of supercooled liquid, and weak MCAO index prevent riming and reduce snowfall rate and mean Ze. This can explain why snowfall, occurs less frequently on 04 April. Moreover, missing riming in updrafts reduces the variability in snowfall rate within each fetch bin. No preconditioning by riming might delay the precipitation onset on 04 April by more than 10 km (Fig. 8p). Hence, precipitation starts forming at fetches of 26 and 39 km on 01 and 04 April, respectively.

5 Conclusions

Our study investigates the evolution of thermodynamics, cloud/circulation morphology, cloud microphysics, and precipitation within the first 170 km fetch (about 4 hours of travel time) during a long-lasting cold air outbreak in the Fram Strait. Airborne remote sensing and in situ observations were performed as part of the HALO-(AC)[3] campaign within two research flights, just three days apart. A unique sampling strategy with research flights oriented perpendicular to cloud streets provided the opportunity to analyze fine-resolved macro- and microphysical cloud and circulation observations in the initial MCAO phase in a statistical sense. Specifically two metrics were developed for this purpose: The first one makes use of a a novel approach to detect roll circulations from vertical radar profiles only. This enables us to composite cloud and precipitation parameters as a function of their position within the roll circulation. The second metric uses back trajectories to analyze the cloud and circulation development with fetch, which allowed us to draw a consistent picture of the MCAO developments on 01 and 04 April 2022 (Fig. 9). Furthermore, the findings help to answer the research questions posed in Sect. 1:

I. What are the differences between the environmental conditions on both flight days, and what are their implications on cloud development?

Both MCAO events feature northerly winds advecting dry and cold air masses into the Fram Strait. The event on 01 April shows colder air temperatures leading to a factor of two stronger MCAO index and stronger heat fluxes. The more active convection on 01 April compared to 04 April deepens the boundary layer, causing higher cloud top heights that
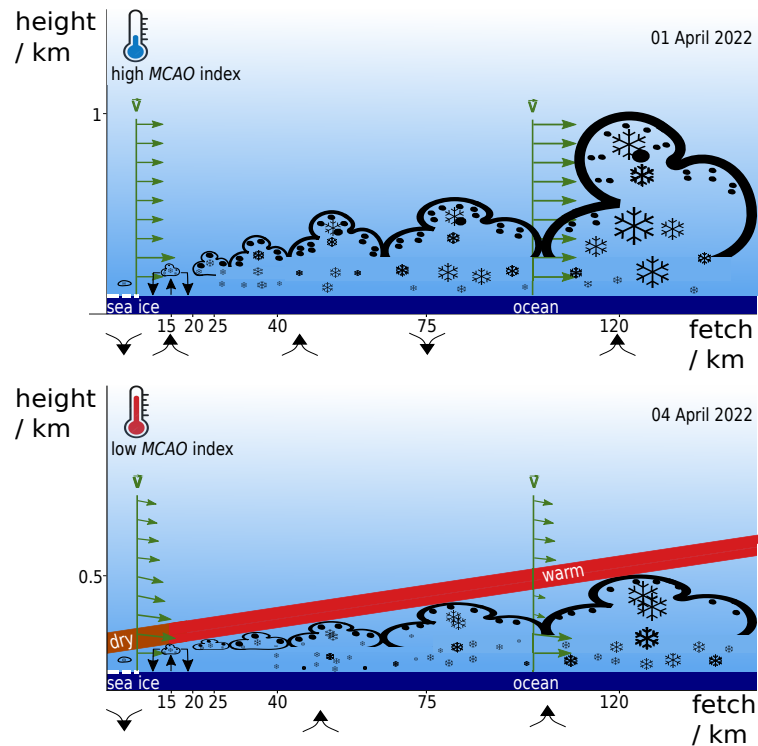
Figure 9. Sketch of the development of roll circulations and microphysics of the associated cloud streets with fetch on 01 April (first row) and 04 April (second row). The arrows at the bottom indicate the direction of the near-surface vertical motion.

are well aligned with the boundary layer height. A rough scaling with a factor of two can be assumed for all parameters between both days. One also has to note that the island of Svalbard influences the flow. This provoked a wave effect in the lee of Svalbard on 01 April with subsiding air masses and thus reduced cloud top heights at 75 to 100 km fetch. On
435   04 April, lee effects caused an even stronger cloud-free zone west of the island, which led to a convergence zone and was not considered in the analysis.

The difference in cloud top height between lidar and radar is used to diagnose the liquid layer thickness LLT, which indicates the presence of supercooled-liquid layer topped mixed-phase clouds for 86% (71%) of the time on 01 (04) April. With respect to cloud microphysics, the most prominent difference between both days is that riming is only significantly
440   active during the cold and strong MCAO case on 01 April. This day also features a higher amount of supercooled liquid water with median liquid water paths of roughly $50\,\mathrm{g\,m^{-2}}$. Riming influences LLT, radar reflectivities, precipitation onset, and strength by producing larger ice particles. Regarding median properties, cloud liquid layer thickness, liquid water path, and snowfall rate are again roughly a factor of two lower for the weaker MCAO on 04 April.

II. Can we identify characteristic changes in cloud and precipitation properties perpendicular to cloud street orientation,
445   i.e., within the roll circulation?

Yes, several hundred roll circulation objects were identified using cloud radar measurements performed on multiple legs perpendicular to cloud street orientation. A composite analysis of these objects reveals that on 01 April, several parameters show consistent trends from the updraft region towards cloud boundaries, while on 04 April, only increased radar reflectivity and precipitation can be found in the updraft region. We hypothesize that the presence of significant riming on 01 April leads to increases in liquid water path, snowfall rate, and the height towards the updraft center while the LLT decreases because updrafts lift ice particles into the pure liquid layer. Our statistical analysis of mean cloud characteristics within the roll circulation and their variability could be used to test the performance of cloud parameterizations and better understand riming effects.

III. How do roll circulation, cloud, and precipitation properties evolve with fetch in the initial MCAO phase, e.g., up to travel times of 4 hours?

Analyzing our measurements as a function of fetch shows increasing cloud top height, liquid water path, radar reflectivity, near-surface precipitation rate, horizontal cloud cover, and fraction of precipitating profiles. Cloud streets form at around 15 km fetch and start precipitating at 25 to 40 km. The later onset of precipitation on 04 April is attributed to the lack of riming. The aspect ratio of the roll circulation decreases with fetch for fetches smaller 50 km and stays constant for larger fetches. The wavelength of the cloud streets λ slightly increases with fetch on 01 April but the variability is rather high. Nevertheless, λ is just barely larger than 1 km within the first 100 km as also found in the spectral analysis of riming. Such small scales are extremely difficult to resolve from space, highlighting the importance of airborne measurements.

To answer the two last research questions, we established composite approaches to characterize the roll circulation (Fig. 7) and fetch (Fig. 8). Such metrics can also be generated from cloud-resolving model output and be used to evaluate their performance to represent microphysics and dynamics in the initial phase of an MCAO. By considering the two cases with similar large-scale synoptic settings but differences with respect to microphysics, e.g., LWP and riming, insights into the simulation of cloud microphysics could be gained. In particular, it will be interesting to analyze whether such models successfully reproduce the observed factor of two in scaling found for several parameters between the two cases.

To study the impact of the sharpness of MIZ and flow divergence on cloud evolution, more observations at constant fetches over open water and variable fetches over MIZ near the sea ice edge must be obtained in the future. Moreover, since the observed cloud top temperatures lie within the dendritic-growth zone, aggregation would be another interesting process to study, which is possible by dual frequency radar observations (Chellini et al., 2022).

The Clouds over cOMPlEX environment (COMPEX) campaign planned for spring 2026 northwest of Svalbard will raise the opportunity to better characterize the impact of the marginal sea ice zone (MIZ) on the air mass transformation. Flights within the MIZ and along the ice edge could increase the number of samples. Further, by enhancing our measurement suite with an airborne G-band radar, more information on cloud microphysics can be deduced.

Data availability. Processed radar, in situ, and dropsonde observations obtained during the HALO-(AC)[3] campaign are published by Ehrlich et al. (2024). The retrieved LWP data are currently being prepared for publication on PANGAEA. All airborne data are accessed via

the ac3airborne module (Mech et al., 2022b). The merged MODIS-AMSR2 sea ice concentration data are provided by the Institute of Environmental Physics at the University of Bremen (Ludwig and Spreen, 2023). Raw in situ data are stored at the German Aerospace Center and available on request. Back trajectories are calculated from ERA5 reanalysis data (Hersbach et al., 2017, 2020). ERA5 is available on pressure levels (Hersbach et al., 2023a) and single levels (Hersbach et al., 2023b). A Python implementation of the COARE 3.5 bulk air-sea flux algorithm is available at Ludovic et al. (2021). MODIS observations of the total water path can be found under Nasa Worldview (2023a) and of corrected reflectance under Nasa Worldview (2023b). The corrected reflectance observed by VIIRS is available at (Nasa Worldview, 2023c).

Appendix A: Peak detection algorithm and sensivity

To detect up- and downdrafts, we solely use $Ze_{0.7}$, which are radar reflectivity measurements at the height of 0.7 of the hydrometeor depth (D; Sec. 2.2). Figure A1 explains the choice of this height (red line). To understand the applied height and Ze thresholds, one has to keep in mind that Ze values larger -5 dBZ (Schirmacher et al., 2023) and below 500 m (Shupe et al., 2008) height are defined as precipitation. At 0.7 of the hydrometeor depth, most largest cloud particles occur, i.e., most maximum Ze per profile exceeding -10 dBZ taken among all non-precipitating values (Fig. A1a, gray line). Most maximum Ze per profile among non-precipitating radar bins occur at cloud bottom (Fig. A1a, black line). Nevertheless, this bottom-near maximum is induced by very small Ze values below -10 dBZ. Since we aim to detect updrafts at the selected height, we take the height where large particles (>-10 dBZ) occur most frequently. Moreover, with 98 %, most precipitation occurs below 0.7 of the hydrometeor depth (Fig. A1b, dashed black line). This finding is not sensitive to the -5 dBZ threshold for precipitation (Fig. A1b, dashed gray line). Dry entrainment and liquid droplets seem rare at 0.7 of the hydrometeor depth since 91 % of the lowest Ze per profile lie above this altitude (Fig. A1b, solid black line). In conclusion, we take Ze at the height of 0.7 of the hydrometeor depth to consider the largest ice particles within the profiles and minimize the influence of dry air entrainment/supercooled liquid water droplets at cloud top and precipitation at the bottom of the hydrometeor depth.

To find up- and downdraft regions using $Ze_{0.7}$, we follow this recipe:

I. Determine 0.7 of D for every profile (Fig. 2b).

II. Average Ze over 100 m in the vertical to reduce noise.

III. Smooth Ze by averaging over 3 s to minimize noise detection (Fig. 2c).

IV. Extract the smoothed $Ze_{0.7}$ at 0.7 of D for each profile, which is the average between 0.65 and 0.75 times D (Fig. 2d, black line).

V. Derive the large-scale background Ze_{back} by averaging $Ze_{0.7}$ over 500 s (~ 40 km; Fig. 2d, gray line).

VI. Determine peaks in $Ze_{0.7}$ using the python package scipy.signal.find_peaks (Virtanen et al., 2020).
If $Ze_{back} \geq 0.67 \, \text{mm}^6 \, \text{m}^{-3}$, find peaks for $Ze_{0.7}$ with a prominence of at least $0.5 \, \text{mm}^6 \, \text{m}^{-3}$ (difference between the height of the peak and its lowest contour line; Fig. 2d, vertical orange line) and a width of at least 2.9 samples (about 230 m horizontal distance; Fig. 2d, horizontal orange line). Note that Fig. 2 shows Ze in logarithmic space while peaks are detected in linear space.
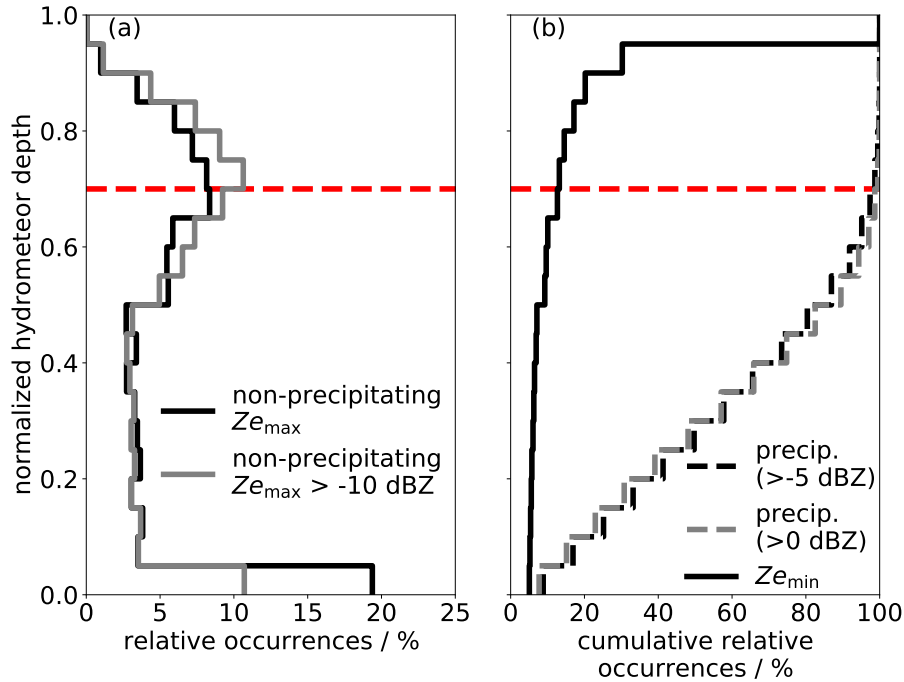
Figure A1. Relative occurrences of Ze_{max} among non-precipitating hydrometeors (a, black solid) and of non-precipitating Ze_{max} that exceed -10 dBZ (a, gray solid). Relative occurrence of precipitation defined by Ze values larger -5 dBZ (b, black dashed) and larger 0 dBZ (b, gray dashed), and minimum Ze of each radar profile (b, black solid). The y-axis is the normalized hydrometeor depth (0=base, 1=top). The height that is used to identify roll circulations is indicated by the red line.

If $Ze_{\mathrm{back}} < 0.67\,\mathrm{mm}^6\,\mathrm{m}^{-3}$, find peaks for $Ze_{0.7}$ with a prominence of at least $0.1\,\mathrm{mm}^6\,\mathrm{m}^{-3}$ and a width of at least 2.9 samples.

The detected peaks are defined as updrafts (Fig. 2e, vertical black lines) Here, we apply two different thresholds depending on Ze_{back} since the magnitude of the averaged Ze and its peaks generally increase with fetch.

VII. Find the minimum $Ze_{0.7}$ between every two maxima (Fig. 2e, vertical gray line). If conditions between two cloud streets are cloud-free, we consider the downdraft location at the center of the cloud-free distance.

Table A1. Sensitivity of the steps of the algorithm applied to identify roll circulation objects. Relative changes of the number of objects in total, number of objects inside the 'cloud street' regime, cloud top height (CTH) of cloud streets, and aspect ratio (AR) of the roll circulation to the results obtained by the applied configuration after adjusting, i.e., mostly doubling, parameters.

modification	total number of objects	number of objects within 'cloud street' regime	CTH	AR
III: average over 6 s	-17.8 %	-20 %	+24 %	+23 %
IV: 0.6 of hydrometeor depth	-1.8 %	-1 %	0 %	0 %
IV: 0.8 of hydrometeor depth	+3.4 %	0 %	0 %	0 %
VI: width of 5.8 samples	-31.3 %	-37 %	+59 %	+57 %
VI: If $Ze_{\mathrm{back}} \geq 0.67\,\mathrm{mm}^6\,\mathrm{m}^{-3}$: prominence of at least $0.2\,\mathrm{mm}^6\,\mathrm{m}^{-3}$	-9.8 %	-11 %	+10 %	+11 %
VI: If $Ze_{\mathrm{back}} < 0.67\,\mathrm{mm}^6\,\mathrm{m}^{-3}$: prominence of at least $1\,\mathrm{mm}^6\,\mathrm{m}^{-3}$	-9.3 %	-10 %	+10 %	+11 %

Author contributions. IS performed the analysis, visualization, and writing and developed the methodology. Together with SS, MK, AE, and SC, the paper was conceptualized, and results were discussed. MM and AE developed the flight strategy for the cloud street investigation. BK calculated the back trajectories. NM collocated the *P5* and *P6* measurements and computed the rime mass fraction. All authors contributed to manuscript revisions.

Competing interests. The authors declare no competing interests.

Acknowledgements. We gratefully acknowledge the funding by the Deutsche Forschungsgemeinschaft (DFG, German Research Foundation) - Projektnummer 268020496 - TRR 172, within the Transregional Collaborative Research Center "ArctiC Amplification: Climate Relevant Atmospheric and SurfaCe Processes, and Feedback Mechanisms (AC)[3]" - in subproject B03. Furthermore, we acknowledge the support for the Article Processing Charge from the DFG (German Research Foundation, 491454339). We are grateful for the support from the Alfred-Wegener-Institute, DLR, and aircraft crews during the HALO-(AC)[3] campaign. Moreover, we acknowledge the use of imagery from the NASA Worldview application (Nasa Worldview, 2023a, b, c), part of the NASA Earth Observing System Data and Information System (EOSDIS). Furthermore, we thank the Institute of Environmental Physics, University of Bremen for providing the merged MODIS-AMSR2 sea ice concentration dataset (Ludwig and Spreen, 2023). Many thanks to the PIs Stephan Borrmann, Johannes Schneider, and Veronika Pörtge. We are also grateful to Bjorn Stevens for discussing the flight strategy and cloud street investigation, Matt Shupe for discussing the roll circulation identification, and Vera Schemann for discussing future model evaluation efforts.

References

Abel, S. J., Boutle, I. A., Waite, K., Fox, S., Brown, P. R. A., Cotton, R., Lloyd, G., Choularton, T. W., and Bower, K. N.: The Role of Precipitation in Controlling the Transition from Stratocumulus to Cumulus Clouds in a Northern Hemisphere Cold-Air Outbreak, Journal of the Atmospheric Sciences, 74, 2293–2314, https://doi.org/10.1175/JAS-D-16-0362.1, 2017.

Atkinson, B. W. and Wu Zhang, J.: Mesoscale shallow convection in the atmosphere, Reviews of Geophysics, 34, 403–431, https://doi.org/10.1029/96RG02623, 1996.

Baumgardner, D., Brenguier, J. L., Bucholtz, A., Coe, H., DeMott, P., Garrett, T. J., Gayet, J. F., Hermann, M., Heymsfield, A., Korolev, A., Krämer, M., Petzold, A., Strapp, W., Pilewskie, P., Taylor, J., Twohy, C., Wendisch, M., Bachalo, W., and Chuang, P.: Airborne instruments to measure atmospheric aerosol particles, clouds and radiation: A cook's tour of mature and emerging technology, Atmospheric Research, 102, 10–29, https://doi.org/10.1016/j.atmosres.2011.06.021, 2011.

Brown, R. A.: On the Inflection Point Instability of a Stratified Ekman Boundary Layer, Journal of the Atmospheric Sciences, 29, 850–859, https://doi.org/10.1175/1520-0469(1972)029<0850:OTIPIO>2.0.CO;2, 1972.

Brummer, B., Schlunzen, H., and Bogel, W.: Cloud streets duringKontur, pp. 63–77, 1982.

Brümmer, B.: Boundary-layer modification in wintertime cold-air outbreaks from the Arctic sea ice, Boundary-Layer Meteorology, 80, 109–125, https://doi.org/10.1007/BF00119014, 1996.

Brümmer, B.: Roll and Cell Convection in Wintertime Arctic Cold-Air Outbreaks, Journal of the Atmospheric Sciences, 56, 2613–2636, https://doi.org/10.1175/1520-0469(1999)056<2613:RACCIW>2.0.CO;2, 1999.

Brümmer, B., Bakan, S., and Hinzpeter, H.: Kontur: Observations of cloud streets and open cellular structures, Dynamics of Atmospheres and Oceans, 9, 281–296, https://doi.org/10.1016/0377-0265(85)90024-7, 1985.

Brümmer, B., Rump, B., and Kruspe, G.: A cold air outbreak near Spitsbergen in springtime — Boundary-layer modification and cloud development, Boundary-Layer Meteorology, 61, 13–46, https://doi.org/10.1007/BF02033993, 1992.

Chellini, G., Gierens, R., and Kneifel, S.: Ice Aggregation in Low-Level Mixed-Phase Clouds at a High Arctic Site: Enhanced by Dendritic Growth and Absent Close to the Melting Level, Journal of Geophysical Research: Atmospheres, 127, https://doi.org/10.1029/2022JD036860, 2022.

Copernicus Marine Service: Arctic Ocean - Sea and Ice Surface Temperature, https://doi.org/10.48670/moi-00130, (last access: 31 October 2023) [data], 2023.

Dahlke, S., Solbès, A., and Maturilli, M.: Cold Air Outbreaks in Fram Strait: Climatology, Trends, and Observations During an Extreme Season in 2020, Journal of Geophysical Research: Atmospheres, 127, e2021JD035741, https://doi.org/10.1029/2021JD035741, 2022.

de Roode, S. R., Frederikse, T., Siebesma, A. P., Ackerman, A. S., Chylik, J., Field, P. R., Fricke, J., Gryschka, M., Hill, A., Honnert, R., Krueger, S. K., Lac, C., Lesage, A. T., and Tomassini, L.: Turbulent Transport in the Gray Zone: A Large Eddy Model Intercomparison Study of the CONSTRAIN Cold Air Outbreak Case, Journal of Advances in Modeling Earth Systems, 11, 597–623, https://doi.org/10.1029/2018MS001443, 2019.

Ehrlich, A., Crewell, S., Herber, A., Klingebiel, M., Lüpkes, C., Mech, M., Becker, S., Borrmann, S., Bozem, H., Buschmann, M., Clemen, H.-C., De La Torre Castro, E., Dorff, H., Dupuy, R., Eppers, O., Ewald, F., George, G., Giez, A., Grawe, S., Gourbeyre, C., Hartmann, J., Jäkel, E., Joppe, P., Jourdan, O., Jurányi, Z., Kirbus, B., Lucke, J., Luebke, A. E., Maahn, M., Maherndl, N., Mallaun, C., Mayer, J., Mertes, S., Mioche, G., Moser, M., Müller, H., Pörtge, V., Risse, N., Roberts, G., Rosenburg, S., Röttenbacher, J., Schäfer, M., Schaefer, J., Schäfler, A., Schirmacher, I., Schneider, J., Schnitt, S., Stratmann, F., Tatzelt, C., Voigt, C., Walbröl, A., Weber, A., Wetzel, B., Wirth,

570   M., and Wendisch, M.: A comprehensive in-situ and remote sensing data set collected during the HALO–(AC)[3] aircraft campaign, Earth System Science Data Discussions, 2024, 1–49, https://doi.org/10.5194/essd-2024-281, 2024.

Fairall, C. W., Bradley, E. F., Hare, J. E., Grachev, A. A., and Edson, J. B.: Bulk Parameterization of Air–Sea Fluxes: Updates and Verification for the COARE Algorithm, Journal of Climate, 16, 571–591, https://doi.org/10.1175/1520-0442(2003)016<0571:BPOASF>2.0.CO;2, publisher: American Meteorological Society Section: Journal of Climate, 2003.

575   Geerts, B., Giangrande, S. E., McFarquhar, G. M., Xue, L., Abel, S. J., Comstock, J. M., Crewell, S., DeMott, P. J., Ebell, K., Field, P., Hill, T. C. J., Hunzinger, A., Jensen, M. P., Johnson, K. L., Juliano, T. W., Kollias, P., Kosovic, B., Lackner, C., Luke, E., Lüpkes, C., Matthews, A. A., Neggers, R., Ovchinnikov, M., Powers, H., Shupe, M. D., Spengler, T., Swanson, B. E., Tjernström, M., Theisen, A. K., Wales, N. A., Wang, Y., Wendisch, M., and Wu, P.: The COMBLE Campaign: A Study of Marine Boundary Layer Clouds in Arctic Cold-Air Outbreaks, Bulletin of the American Meteorological Society, 103, E1371–E1389, https://doi.org/10.1175/BAMS-D-21-0044.1, 2022.

580   George, G., Stevens, B., Bony, S., Pincus, R., Fairall, C., Schulz, H., Kölling, T., Kalen, Q. T., Klingebiel, M., Konow, H., Lundry, A., Prange, M., and Radtke, J.: JOANNE: Joint dropsonde Observations of the Atmosphere in tropical North atlaNtic meso-scale Environments, Earth Syst. Sci. Data, 13, 5253–5272, https://doi.org/10.5194/essd-13-5253-2021, 2021.

Gryschka, M., Fricke, J., and Raasch, S.: On the impact of forced roll convection on vertical turbulent transport in cold air outbreaks, Journal of Geophysical Research: Atmospheres, 119, 12–513, 2014.

585   Hersbach, H., Bell, B., Berrisford, P., Hirahara, S., Horányi, A., Muñoz-Sabater, J., Nicolas, J., Peubey, C., Radu, R., Schepers, D., Simmons, A., Soci, C., Abdalla, S., Abellan, X., Balsamo, G., Bechtold, P., Biavati, G., Bidlot, J., Bonavita, M., De Chiara, G., Dahlgren, P., Dee, D., Diamantakis, M., Dragani, R., Flemming, J., Forbes, R., Fuentes, M., Geer, A., Haimberger, L., Healy, S., Hogan, R. J., Hólm, E., Janisková, M., Keeley, S., Laloyaux, P., Lopez, P., Lupu, C., Radnoti, G., de Rosnay, P., Rozum, I., Vamborg, F., Villaume, S., and Thépaut, J.-N.: Complete ERA5 from 1940: Fifth generation of ECMWF atmospheric reanalyses of the global climate, Copernicus Climate Change

590   Service (C3S) Data Store (CDS), https://doi.org/10.24381/cds.143582cf, (last access: 03 November 2023) [data], 2017.

Hersbach, H., Bell, B., Berrisford, P., Hirahara, S., Horányi, A., Muñoz-Sabater, J., Nicolas, J., Peubey, C., Radu, R., Schepers, D., Simmons, A., Soci, C., Abdalla, S., Abellan, X., Balsamo, G., Bechtold, P., Biavati, G., Bidlot, J., Bonavita, M., De Chiara, G., Dahlgren, P., Dee, D., Diamantakis, M., Dragani, R., Flemming, J., Forbes, R., Fuentes, M., Geer, A., Haimberger, L., Healy, S., Hogan, R. J., Hólm, E., Janisková, M., Keeley, S., Laloyaux, P., Lopez, P., Lupu, C., Radnoti, G., de Rosnay, P., Rozum, I., Vamborg, F., Vil-

595   laume, S., and Thépaut, J.-N.: The ERA5 global reanalysis, Quarterly Journal of the Royal Meteorological Society, 146, 1999–2049, https://doi.org/10.1002/qj.3803, 2020.

Hersbach, H., Bell, B., Berrisford, P., Biavati, G., Horányi, A., Muñoz Sabater, J., Nicolas, J., Peubey, C., Radu, R., Rozum, I., Schepers, D., Simmons, A., Soci, C., Dee, D., and Thépaut, J.-N.: ERA5 hourly data on pressure levels from 1940 to present, Copernicus Climate Change Service (C3S) Climate Data Store (CDS), https://doi.org/10.24381/cds.bd0915c6, (last access: 29 August 2024) [data], 2023a.

600   Hersbach, H., Bell, B., Berrisford, P., Biavati, G., Horányi, A., Muñoz Sabater, J., Nicolas, J., Peubey, C., Radu, R., Rozum, I., Schepers, D., Simmons, A., Soci, C., Dee, D., and Thépaut, J.-N.: ERA5 hourly data on single levels from 1940 to present, Copernicus Climate Change Service (C3S) Climate Data Store (CDS), https://doi.org/10.24381/cds.adbb2d47, (last access: 29 August 2024) [data], 2023b.

Kirbus, B., Schirmacher, I., Klingebiel, M., Schäfer, M., Ehrlich, A., Slättberg, N., Lucke, J., Moser, M., Müller, H., and Wendisch, M.: Thermodynamic and cloud evolution in a cold air outbreak during HALO-(AC)[3]: Quasi-Lagrangian observations compared to the ERA5

605   and CARRA reanalyses, EGUsphere, pp. 1–40, https://doi.org/10.5194/egusphere-2023-2989, 2023.

Klingebiel, M., de Lozar, A., Molleker, S., Weigel, R., Roth, A., Schmidt, L., Meyer, J., Ehrlich, A., Neuber, R., Wendisch, M., and Borrmann, S.: Arctic low-level boundary layer clouds: in situ measurements and simulations of mono- and bimodal supercooled droplet size distribu-

tions at the top layer of liquid phase clouds, Atmospheric Chemistry and Physics, 15, 617–631, https://doi.org/10.5194/acp-15-617-2015, 2015.

610 Kolstad, E. W.: Higher ocean wind speeds during marine cold air outbreaks, Quarterly Journal of the Royal Meteorological Society, 143, 2084–2092, https://doi.org/10.1002/qj.3068, 2017.

Korolev, A. and Field, P. R.: The effect of dynamics on mixed-phase clouds: Theoretical considerations, Journal of the Atmospheric Sciences, 65, 66–86, 2008.

Kulie, M. S. and Bennartz, R.: Utilizing Spaceborne Radars to Retrieve Dry Snowfall, Journal of Applied Meteorology and Climatology, 48, 615 2564–2580, https://doi.org/10.1175/2009JAMC2193.1, 2009.

Lackner, C. P., Geerts, B., Juliano, T. W., Xue, L., and Kosovic, B.: Vertical structure of clouds and precipitation during Arctic cold-air outbreaks and warm-air intrusions: Observations from COMBLE, Journal of Geophysical Research: Atmospheres, 128, e2022JD038403, 2023.

Lance, S., Brock, C. A., Rogers, D., and Gordon, J. A.: Water droplet calibration of the Cloud Droplet Probe (CDP) and in-620 flight performance in liquid, ice and mixed-phase clouds during ARCPAC, Atmospheric Measurement Techniques, 3, 1683–1706, https://doi.org/10.5194/amt-3-1683-2010, 2010.

Li, X., Krueger, S. K., Strong, C., Mace, G. G., and Benson, S.: Midwinter Arctic leads form and dissipate low clouds, Nature Communications, 11, 206, https://doi.org/10.1038/s41467-019-14074-5, 2020.

Ludovic, B., Byron, B., Christopher, F., Elizabeth, T., Jim, E., and Robert, P.: Python implementation of the COARE 3.5 Bulk Air- Sea Flux 625 algorithm, https://doi.org/10.5281/zenodo.5110991, 2021.

Ludwig, V. and Spreen, G.: modis_amsr2, https://data.seaice.uni-bremen.de/modis_amsr2/, (last access: 20 October 2023) [data], 2023.

Ludwig, V., Spreen, G., and Pedersen, L. T.: Evaluation of a New Merged Sea-Ice Concentration Dataset at 1 km Resolution from Thermal Infrared and Passive Microwave Satellite Data in the Arctic, Remote Sensing, 12, 3183, https://doi.org/10.3390/rs12193183, 2020.

Maahn, M., Burgard, C., Crewell, S., Gorodetskaya, I. V., Kneifel, S., Lhermitte, S., Van Tricht, K., and van Lipzig, N. P. M.: How does the 630 spaceborne radar blind zone affect derived surface snowfall statistics in polar regions?, Journal of Geophysical Research: Atmospheres, 119, 13,604–13,620, https://doi.org/10.1002/2014JD022079, _eprint: https://onlinelibrary.wiley.com/doi/pdf/10.1002/2014JD022079, 2014.

Mages, Z., Kollias, P., Zhu, Z., and Luke, E. P.: Surface-based observations of cold-air outbreak clouds during the COMBLE field campaign, preprint, https://doi.org/10.5194/acp-2022-546, 2022.

635 Maherndl, N., Maahn, M., Tridon, F., Leinonen, J., Ori, D., and Kneifel, S.: A riming-dependent parameterization of scattering by snowflakes using the self-similar Rayleigh–Gans approximation, Quarterly Journal of the Royal Meteorological Society, pp. 1–20, https://doi.org/10.1002/qj.4573, 2023a.

Maherndl, N., Moser, M., Lucke, J., Mech, M., Risse, N., Schirmacher, I., and Maahn, M.: Quantifying riming from airborne data during HALO-(AC)[3], EGUsphere, pp. 1–32, https://doi.org/10.5194/egusphere-2023-1118, 2023b.

640 Markson, R.: Atmospheric Electrical Detection of Organized Convection, American Association for the Advancement of Science, pp. 1171 – 1177, https://doi.org/10.1126/science.188.4194.1171, 1975.

Mateling, M. E., Pettersen, C., Kulie, M. S., and L'Ecuyer, T. S.: Marine Cold-Air Outbreak Snowfall in the North Atlantic: A CloudSat Perspective, Journal of Geophysical Research: Atmospheres, 128, https://doi.org/10.1029/2022JD038053, 2023.

Mech, M., Kliesch, L.-L., Anhäuser, A., Rose, T., Kollias, P., and Crewell, S.: Microwave Radar/radiometer for Arctic Clouds (MiRAC):
645   first insights from the ACLOUD campaign, Atmospheric Measurement Techniques, 12, 5019–5037, https://doi.org/10.5194/amt-12-5019-
           2019, 2019.

Mech, M., Ehrlich, A., Herber, A., Lüpkes, C., Wendisch, M., Becker, S., Boose, Y., Chechin, D., Crewell, S., Dupuy, R., Gourbeyre, C.,
           Hartmann, J., Jäkel, E., Jourdan, O., Kliesch, L.-L., Klingebiel, M., Kulla, B. S., Mioche, G., Moser, M., Risse, N., Ruiz-Donoso, E.,
           Schäfer, M., Stapf, J., and Voigt, C.: MOSAiC-ACA and AFLUX - Arctic airborne campaigns characterizing the exit area of MOSAiC,
650   Scientific Data, 9, 790, https://doi.org/10.1038/s41597-022-01900-7, 2022a.

Mech, M., Risse, N., Marrollo, G., and Paul, D.: Ac3airborne, 10.5281/zenodo.7305585, [code], 2022b.

Morrison, H., de Boer, G., Feingold, G., Harrington, J., Shupe, M. D., and Sulia, K.: Resilience of persistent Arctic mixed-phase clouds,
           Nature Geoscience, 5, 11–17, https://doi.org/10.1038/ngeo1332, 2012.

Moser, M., Voigt, C., Jurkat-Witschas, T., Hahn, V., Mioche, G., Jourdan, O., Dupuy, R., Gourbeyre, C., Schwarzenboeck, A., Lucke, J.,
655   Boose, Y., Mech, M., Borrmann, S., Ehrlich, A., Herber, A., Lüpkes, C., and Wendisch, M.: Microphysical and thermodynamic phase anal-
           yses of Arctic low-level clouds measured above the sea ice and the open ocean in spring and summer, preprint, https://doi.org/10.5194/acp-
           2023-44, 2023.

Murray-Watson, R. J., Gryspeerdt, E., and Goren, T.: Investigating the development of clouds within marine cold air outbreaks, EGUsphere,
           pp. 1–29, https://doi.org/10.5194/egusphere-2023-734, 2023.

660 Müller, G., Brümmer, B., and Alpers, W.: Roll Convection within an Arctic Cold-Air Outbreak: Interpretation of In Situ Aircraft Mea-
           surements and Spaceborne SAR Imagery by a Three-Dimensional Atmospheric Model, Monthly Weather Review, 127, 363–380,
           https://doi.org/10.1175/1520-0493(1999)127<0363:RCWAAC>2.0.CO;2, 1999.

Nasa Worldview: Cloud Water Path Terra / MODIS, https://go.nasa.gov/46vE70B, (last access: 21 November 2023), 2023a.

Nasa Worldview: Corrected Reflectance (True Color) Terra / MODIS, https://go.nasa.gov/46o4aXO, (last access: 21 November 2023), 2023b.

665 Nasa Worldview: Corrected Reflectance (Bands M3-I3-M11) Suomi NPP / VIIRS, https://go.nasa.gov/47mKJjr, (last access: 21 November
           2023), 2023c.

Papritz, L., Pfahl, S., Sodemann, H., and Wernli, H.: A Climatology of Cold Air Outbreaks and Their Impact on Air–Sea Heat Fluxes in the
           High-Latitude South Pacific, Journal of Climate, 28, 342–364, https://doi.org/10.1175/JCLI-D-14-00482.1, 2015.

Pithan, F., Svensson, G., Caballero, R., Chechin, D., Cronin, T. W., Ekman, A. M. L., Neggers, R., Shupe, M. D., Solomon, A., Tjernström,
670   M., and Wendisch, M.: Role of air-mass transformations in exchange between the Arctic and mid-latitudes, Nature Geoscience, 11, 805–
           812, https://doi.org/10.1038/s41561-018-0234-1, 2018.

Ruiz-Donoso, E., Ehrlich, A., Schäfer, M., Jäkel, E., Schemann, V., Crewell, S., Mech, M., Kulla, B. S., Kliesch, L.-L., Neuber, R., and
           Wendisch, M.: Small-scale structure of thermodynamic phase in Arctic mixed-phase clouds observed by airborne remote sensing during
           a cold air outbreak and a warm air advection event, Atmospheric Chemistry and Physics, 20, 5487–5511, https://doi.org/10.5194/acp-20-
675   5487-2020, 2020.

Schirmacher, I., Kollias, P., Lamer, K., Mech, M., Pfitzenmaier, L., Wendisch, M., and Crewell, S.: Assessing Arctic low-level clouds and
           precipitation from above – a radar perspective, Atmospheric Measurement Techniques, 16, 4081–4100, https://doi.org/10.5194/amt-16-
           4081-2023, 2023.

Shupe, M. D., Kollias, P., Persson, P. O. G., and McFarquhar, G. M.: Vertical Motions in Arctic Mixed-Phase Stratiform Clouds, Journal of
680   the Atmospheric Sciences, 65, 1304–1322, https://doi.org/10.1175/2007JAS2479.1, 2008.

Spensberger, C. and Spengler, T.: Sensitivity of Air-Sea Heat Exchange in Cold-Air Outbreaks to Model Resolution and Sea-Ice Distribution, Journal of Geophysical Research: Atmospheres, 126, https://doi.org/10.1029/2020JD033610, 2021.

Sprenger, M. and Wernli, H.: The LAGRANTO Lagrangian analysis tool – version 2.0, Geoscientific Model Development, 8, 2569–2586, https://doi.org/10.5194/gmd-8-2569-2015, 2015.

Stachlewska, I. S., Neuber, R., Lampert, A., Ritter, C., and Wehrle, G.: AMALi – the Airborne Mobile Aerosol Lidar for Arctic research, Atmos. Chem. Phys., p. 17, https://doi.org/10.5194/acp-10-2947-2010, 2010.

Tornow, F., Ackerman, A. S., and Fridlind, A. M.: Preconditioning of overcast-to-broken cloud transitions by riming in marine cold air outbreaks, Atmospheric Chemistry and Physics, 21, 12 049–12 067, https://doi.org/10.5194/acp-21-12049-2021, 2021.

Turner, J. and Marshall, G. J.: Climate change in the polar regions, Cambridge University Press, https://books.google.de/books?id=klTlaWWWxNoC, 2011.

Vaisala: Vaisala Dropsonde RD94, https://www.vaisala.com/sites/default/files/documents/RD94-Dropsonde-Datasheet-B210936EN-A-LoRes.pdf, (last access: 31 October 2023), 2010.

Virtanen, P., Gommers, R., Oliphant, T. E., Haberland, M., Reddy, T., Cournapeau, D., Burovski, E., Peterson, P., Weckesser, W., Bright, J., van der Walt, S. J., Brett, M., Wilson, J., Millman, K. J., Mayorov, N., Nelson, A. R. J., Jones, E., Kern, R., Larson, E., Carey, C. J., Polat, İ., Feng, Y., Moore, E. W., VanderPlas, J., Laxalde, D., Perktold, J., Cimrman, R., Henriksen, I., Quintero, E. A., Harris, C. R., Archibald, A. M., Ribeiro, A. H., Pedregosa, F., van Mulbregt, P., and SciPy 1.0 Contributors: SciPy 1.0: Fundamental Algorithms for Scientific Computing in Python, Nature Methods, 17, 261–272, https://doi.org/10.1038/s41592-019-0686-2, 2020.

von Lerber, A., Mech, M., Rinke, A., Zhang, D., Lauer, M., Radovan, A., Gorodetskaya, I., and Crewell, S.: Evaluating seasonal and regional distribution of snowfall in regional climate model simulations in the Arctic, Atmospheric Chemistry and Physics, 22, 7287–7317, https://doi.org/10.5194/acp-22-7287-2022, 2022.

Walbröl, A., Michaelis, J., Becker, S., Dorff, H., Ebell, K., Gorodetskaya, I., Heinold, B., Kirbus, B., Lauer, M., Maherndl, N., Maturilli, M., Mayer, J., Müller, H., Neggers, R. A. J., Paulus, F. M., Röttenbacher, J., Rückert, J. E., Schirmacher, I., Slättberg, N., Ehrlich, A., Wendisch, M., and Crewell, S.: Contrasting extremely warm and long-lasting cold air anomalies in the North Atlantic sector of the Arctic during the HALO-$(\mathcal{AC})^3$ campaign, Atmospheric Chemistry and Physics, 24, 8007–8029, https://doi.org/10.5194/acp-24-8007-2024, 2024.

Walter, B. A. and Overland, J. E.: Observations of Longitudinal Rolls in a Near Neutral Atmosphere, Monthly Weather Review, 112, 200–208, https://doi.org/10.1175/1520-0493(1984)112<0200:OOLRIA>2.0.CO;2, 1984.

Wendisch, M., Handorf, D., Tegen, I., Neggers, R., and Spreen, G.: Glimpsing the Ins and Outs of the Arctic Atmospheric Cauldron, Eos, 102, https://doi.org/https://doi.org/10.1029/2021EO155959, 2021.

Wendisch, M., Brückner, M., Crewell, S., Ehrlich, A., Notholt, J., Lüpkes, C., Macke, A., Burrows, J. P., Rinke, A., Quaas, J., Maturilli, M., Schemann, V., Shupe, M. D., Akansu, E. F., Barrientos-Velasco, C., Bärfuss, K., Blechschmidt, A.-M., Block, K., Bougoudis, I., Bozem, H., Böckmann, C., Bracher, A., Bresson, H., Bretschneider, L., Buschmann, M., Chechin, D. G., Chylik, J., Dahlke, S., Deneke, H., Dethloff, K., Donth, T., Dorn, W., Dupuy, R., Ebell, K., Egerer, U., Engelmann, R., Eppers, O., Gerdes, R., Gierens, R., Gorodetskaya, I. V., Gottschalk, M., Griesche, H., Gryanik, V. M., Handorf, D., Harm-Altstädter, B., Hartmann, J., Hartmann, M., Heinold, B., Herber, A., Herrmann, H., Heygster, G., Höschel, I., Hofmann, Z., Hölemann, J., Hünerbein, A., Jafariserajehlou, S., Jäkel, E., Jacobi, C., Janout, M., Jansen, F., Jourdan, O., Jurányi, Z., Kalesse-Los, H., Kanzow, T., Käthner, R., Kliesch, L. L., Klingebiel, M., Knudsen, E. M., Kovács, T., Körtke, W., Krampe, D., Kretzschmar, J., Kreyling, D., Kulla, B., Kunkel, D., Lampert, A., Lauer, M., Lelli, L., Lerber, A. v., Linke, O., Löhnert, U., Lonardi, M., Losa, S. N., Losch, M., Maahn, M., Mech, M., Mei, L., Mertes, S., Metzner, E., Mewes, D., Michaelis, J., Mioche, G., Moser, M., Nakoudi, K., Neggers, R., Neuber, R., Nomokonova, T., Oelker, J., Papakonstantinou-Presvelou, I., Pätzold,

720 F., Pefanis, V., Pohl, C., Pinxteren, M. v., Radovan, A., Rhein, M., Rex, M., Richter, A., Risse, N., Ritter, C., Rostosky, P., Rozanov, V. V., Donoso, E. R., Garfias, P. S., Salzmann, M., Schacht, J., Schäfer, M., Schneider, J., Schnierstein, N., Seifert, P., Seo, S., Siebert, H., Soppa, M. A., Spreen, G., Stachlewska, I. S., Stapf, J., Stratmann, F., Tegen, I., Viceto, C., Voigt, C., Vountas, M., Walbröl, A., Walter, M., Wehner, B., Wex, H., Willmes, S., Zanatta, M., and Zeppenfeld, S.: Atmospheric and Surface Processes, and Feedback Mechanisms Determining Arctic Amplification: A Review of First Results and Prospects of the (AC)3 Project, Bulletin of the American Meteorological Society, 104, E208–E242, https://doi.org/10.1175/BAMS-D-21-0218.1, 2023.

725 Wendisch, M., Crewell, S., Ehrlich, A., Herber, A., Kirbus, B., Lüpkes, C., Mech, M., Abel, S. J., Akansu, E. F., Ament, F., Aubry, C., Becker, S., Borrmann, S., Bozem, H., Brückner, M., Clemen, H.-C., Dahlke, S., Dekoutsidis, G., Delanoë, J., De La Torre Castro, E., Dorff, H., Dupuy, R., Eppers, O., Ewald, F., George, G., Gorodetskaya, I. V., Grawe, S., Groß, S., Hartmann, J., Henning, S., Hirsch, L., Jäkel, E., Joppe, P., Jourdan, O., Jurányi, Z., Karalis, M., Kellermann, M., Klingebiel, M., Lonardi, M., Lucke, J., Luebke, A., Maahn, M., Maherndl, N., Maturilli, M., Mayer, B., Mayer, J., Mertes, S., Michaelis, J., Michalkov, M., Mioche, G., Moser, M., Müller, H., Neggers, R., Ori, 730 D., Paul, D., Paulus, F., Pilz, C., Pithan, F., Pöhlker, M., Pörtge, V., Ringel, M., Risse, N., Roberts, G. C., Rosenburg, S., Röttenbacher, J., Rückert, J., Schäfer, M., Schäfer, J., Schemannn, V., Schirmacher, I., Schmidt, J., Schmidt, S., Schneider, J., Schnitt, S., Schwarz, A., Siebert, H., Sodemann, H., Sperzel, T., Spreen, G., Stevens, B., Stratmann, F., Svensson, G., Tatzelt, C., Tuch, T., Vihma, T., Voigt, C., Volkmer, L., Walbröl, A., Weber, A., Wehner, B., Wetzel, B., Wirth, M., and Zinner, T.: Overview: Quasi-Lagrangian observations of Arctic air mass transformations – Introduction and initial results of the HALO–(AC)[3] aircraft campaign, EGUsphere, 2024, 1–46, 735 https://doi.org/10.5194/egusphere-2024-783, 2024.

Wesche, C., Steinhage, D., and Nixdorf, U.: Polar aircraft Polar5 and Polar6 operated by the Alfred Wegener Institute, Journal of large-scale research facilities JLSRF, 2, A87–A87, https://doi.org/10.17815/jlsrf-2-153, 2016.

Ziereis, H. and Gläßer, M.: HALO - Global Player für die Atmosphärenforschung, DLR Nachrichten, pp. 32–36, 2006.